The Astronomical Journal, 168:60 (18pp), 2024 August https://doi.org/10.3847/1538-3881/ad4edf

Evolution of Flare Activity in GKM Stars Younger Than 300 Myr over Five Years of TESS Observations

Adina D. Feinstein[1,8], Darryl Z. Seligman[2,9], Kevin France[1,3,4], Jonathan Gagné[5,6], and Adam Kowalski[3,7]
[1] Laboratory for Atmospheric and Space Physics, University of Colorado Boulder, UCB 600, Boulder, CO 80309, USA
[2] Department of Astronomy and Carl Sagan Institute, Cornell University, 122 Sciences Drive, Ithaca, NY 14853, USA
[3] Department of Astrophysical and Planetary Sciences, University of Colorado, UCB 389, Boulder, CO 80309, USA
[4] Center for Astrophysics and Space Astronomy, University of Colorado, 389 UCB, Boulder, CO 80309, USA
[5] Planétarium de Montréal, Espace pour la Vie, 4801 av. Pierre-de Coubertin, Montréal, Québec, Canada
[6] Trottier Institute for Research on Exoplanets, Université de Montréal, Département de Physique, C.P. 6128 Succ. Centre-ville, Montréal, QC H3C 3J7, Canada
[7] National Solar Observatory, University of Colorado Boulder, 3665 Discovery Drive, Boulder, CO 80303, USA
Received 2024 January 23; revised 2024 April 30; accepted 2024 May 14; published 2024 July 8

Abstract

Stellar flares are short-duration (< hours) bursts of radiation associated with surface magnetic reconnection events. Stellar magnetic activity generally decreases as a function of both the age and Rossby number, R_0, a measure of the relative importance of the convective and rotational dynamos. Young stars (<300 Myr) have typically been overlooked in population-level flare studies due to challenges with flare-detection methods. Here, we select a sample of stars that are members of 26 nearby moving groups, clusters, or associations with ages <300 Myr that have been observed by the Transiting Exoplanet Survey Satellite at 2 minute cadence. We identified 26,355 flares originating from 3160 stars and robustly measured the rotation periods of 1847 stars. We measure and find the flare frequency distribution slope, α, saturates for all spectral types at $\alpha \sim -0.5$ and is constant over 300 Myr. Additionally, we find that flare rates for stars $t_{\rm age} = 50$–250 Myr are saturated below $R_0 < 0.14$, which is consistent with other indicators of magnetic activity. We find evidence of annual flare rate variability in eleven stars, potentially correlated with long-term stellar activity cycles. Additionally, we crossmatch our entire sample with the Galaxy Evolution Explorer and find no correlation between flare rate and far- and near-ultraviolet flux. Finally, we find the flare rates of planet-hosting stars are relatively lower than comparable, larger samples of stars, which may have ramifications for the atmospheric evolution of short-period exoplanets.

Unified Astronomy Thesaurus concepts: Pre-main sequence stars (1290); Optical flares (1166); Stellar rotation (1629); Stellar activity (1580); Time series analysis (1916)

1. Introduction

Stellar flares are the radiation component of magnetic reconnection events (Benz & Güdel 2010). Such events are readily seen on the Sun (Carrington 1859; Lu & Hamilton 1991; Fletcher et al. 2011), particularly during the maximum in the solar cycle (Webb & Howard 1994). Solar flares can be used as proxies for magnetic activity occurring on other stars (Feigelson & Montmerle 1999; Berdyugina 2005; Kowalski et al. 2010; Feinstein et al. 2022b). Additionally, these short-duration flaring events can have significant ramifications on the evolution of short-period extrasolar planets (France et al. 2016; Günther et al. 2020; Chen et al. 2021). While stellar flares are typically not spatially resolvable, they do lend themselves to characterization via spectroscopic and photometric signatures. Spectroscopic characterization of stellar flares informs our understanding of nonthermal processes affiliated with such events such as coronal mass ejections (Argiroffi et al. 2019; Vida et al. 2019), proton beams (Orrall & Zirker 1976; Woodgate et al. 1992), and accelerated electrons (Osten et al. 2005; Smith et al. 2005).

Photometric observations of stars are more readily available now with exoplanet transit discovery missions and allow us to statistically characterize flare rates and energies at optical/near-infrared wavelengths. Observations of M dwarfs with the Sloan Digital Sky Survey revealed a correlation between the flaring fraction of stars with height above the galactic plane, a proxy for age (Kowalski et al. 2009; Hilton et al. 2010). More recently, NASA's Kepler, K2, and the Transiting Exoplanet Survey Satellite (TESS) missions have provided a wealth of stellar variability data in addition to their primary objective of detecting transiting exoplanets. Flares can be identified within time-series photometry by a sharp rise and subsequent exponential decay in flux, with the latter corresponding to the cooling rate (Kowalski et al. 2013). Kepler (Borucki et al. 2010) provided long-baseline high-cadence observations used to identify stellar flares. There have been extensive studies of flares in Kepler data, from the statistics of superflares on solar-type stars (e.g., Notsu et al. 2013; Shibayama et al. 2013; Maehara et al. 2015; Okamoto et al. 2021) to low-mass stars (e.g., Hawley et al. 2014; Silverberg et al. 2016). Davenport et al. (2019) found that flare activity decreased with increasing rotation period for 347 GKM stars. However, the flare frequency distribution (FFD) slope did not vary significantly as a function of age. As a caveat, the ages of the stars in this study were determined based on their rotation periods, relying on the assumption that gyrochronology alone accurately ages stars.

[8] NHFP Sagan Fellow.
[9] NSF Astronomy and Astrophysics Postdoctoral Fellow.

K2 provided 70 days of baseline observations for a handful of young stars in groups such as Upper Scorpius, Pleiades, Hyades, and Praespe clusters. Ilin et al. (2019, 2021) analyzed flares from K and M stars in these clusters and found that the overall flare activity decreased as a function of age. Moreover, this relationship was steeper for more massive stars in the sample. Paudel et al. (2018) surveyed 10 M6–L0 dwarfs observed with K2 and found the L0 dwarfs had significantly shallower FFDs than the M dwarfs. They found that, on average, young targets (defined by the tangential velocity of the star) exhibited more flares overall. More recently, TESS (Ricker et al. 2015) has provided near-all-sky photometric observations at 30 minute cadence or less. This observing strategy has allowed for more detailed studies of young stellar flares from nearby, dispersed young moving groups and associations. These data permit detailed studies of individual stars, for example characterizing eight superflares ($E_f > 10^{34}$ erg) on the young star AB Doradus over ~60 days of continuous observations (Schmitt et al. 2019), as well as statistical studies of flares across a range of spectral types and ages (Doyle et al. 2020; Feinstein et al. 2022b; Pietras et al. 2022; Yang et al. 2023b).

The 11 yr solar activity cycle represents a change in the magnetic activity of the Sun and manifests itself in a variety of observables including increases in the total number of sunspots (Clette et al. 2014; Kilcik et al. 2014), flares, and coronal mass ejections (Crosby et al. 1993; Webb & Howard 1994; Lin et al. 2023), and an increase in the total solar irradiance (Lean 1987). Insights into the long-term activity cycles of other stars have been limited to photometric and spectroscopic monitoring (Saar & Brandenburg 1999). Lehtinen et al. (2016) collected 16–27 yr of *B*- and *V*-band photometry for 21 young active solar-type stars. They found evidence of long-term stellar activity cycles in 18 targets for which $P_{\rm rot}/P_{\rm cycle} \propto R_0^{-1}$, where $P_{\rm rot}$ is the rotation period, $P_{\rm cycle}$ is the period of the stellar activity cycle, and R_0 is the Rossby number. Additionally, 50 yr of spectroscopic observations of HD 166620 from the Mount Wilson Observatory and Keck revealed both a ~16 yr periodicity in emission from the core of the Ca II H and K lines (Oláh et al. 2016) and evidence that this star entered a grand minimum (Baum et al. 2022). A more complete review of the state of stellar activity cycles can be found in Jeffers et al. (2023) and Işık et al. (2023).

In addition to photometric and spectroscopic observations, solar flares trace the length of the solar activity cycle. The high-cadence observations from Kepler (4 yr baseline) and TESS (currently 5 yr baseline) provide sufficient data for searches of stellar activity cycles from the variations in stellar flare rates. Davenport et al. (2020) demonstrated that the flare rate and FFDs of GJ 1234 has not changed appreciably over 10 yr of observations with both Kepler and TESS. On the other hand, Scoggins et al. (2019) found that the M3V star KIC 8507979 showed a clear decline in flare rate and change in FFD over 4 yr of Kepler observations. While it is not expected to find flare rate and distribution variations in all stars given detection limitations, KIC 8507979 demonstrates the ability to study long-term flare variability as a potential tracer for stellar activity cycles.

The paper is presented as follows. In Section 2, we describe our sample and stellar flare and rotation period identification methods. In Section 3, we present our FFD fits as a function of the stellar age, $T_{\rm eff}$, and R_0. In Section 4, we present evidence of flare rate changes over the 5 yr TESS baseline in eleven young stars, likely correlated with long-term stellar activity cycles. In Section 5, we search for correlations in flare rates with far-ultraviolet (FUV) and near-ultraviolet (NUV) observations from Galaxy Evolution Explorer (GALEX) and place the flare rates of young planet-hosting stars in the context of our broader sample. We conclude in Section 6. We provide additional figures and tables in the Appendix.

This paper was written using the *showyourwork!* open-source software package. The objective of *showyourwork!* is to improve the reproducibility and transparency of scientific research by compiling the manuscript and figures simultaneously. All of the data in this work is hosted on GitHub[10] and Zenodo at doi:10.5281/zenodo.11205821. At the end of every caption figure in this manuscript, there is a GitHub icon (), which links to the Python script used to create that figure.

2. TESS Light Curve Characterization

Here, we provide an overview of the methodology used in this paper. Specifically, we describe the sample selection in Section 2.1, TESS light curve analysis in Section 2.2, flare identification in Section 2.3, flare fitting parameters in Section 2.4, flare quality checks in Section 2.5, and stellar rotation period measurements in Section 2.6.

2.1. Sample Selection

A primary goal of this paper is to measure the relationship between the flare rates and ages of stars. We are particularly interested in this dependency for young stars with ages $4 \leqslant t_{\rm age} \leqslant 300$ Myr. To this end, we used the MOCA database (J. Gagné et al. 2024, in preparation)[11] to identify 26 nearby, aged, young moving groups, associations, and open clusters from which we created our sample of stars. The final targets were required to be: (i) confirmed members, (ii) high-likelihood candidate members, or (iii) candidate members. Membership in these groups has been primarily determined using kinematic information from Gaia (Gaia Collaboration et al. 2016, 2018). The membership status is determined by the probability that BANYAN-Σ assigns based on how well the kinematics of the target matches with the kinematics of the group (Gagné et al. 2018b). These rather stringent cuts resulted in a catalog of 30,889 stars across 26 associations. We summarize the sample and ages for each association (and therefore star) in Table 1.

2.2. TESS Light Curves

We crossmatched our MOCA database sample with the TESS Input Catalog (TIC) based on their Gaia Data Release 2 R.A. and decl.; we required that the distance between the target and the nearest TIC target was within $<1''$. We downselected our sample to stars that have been observed with TESS at 2 minute cadence. This ensures that we are able to temporally resolve and accurately measure the properties of flares for each of these stars (Howard & MacGregor 2022).

This process provided a final sample of 6824 unique targets. These targets have each been observed at a 2 minute cadence between TESS Sector 1 and Sector 67; Sector 67 was the latest available sector at the time that this analysis was performed. In

[10] The GitHub is hyperlinked in the *showyourwork!* stamp at the top of the first page of this manuscript, and can also be found here: https://github.com/afeinstein20/young-stellar-flares.

[11] https://mocadb.ca/

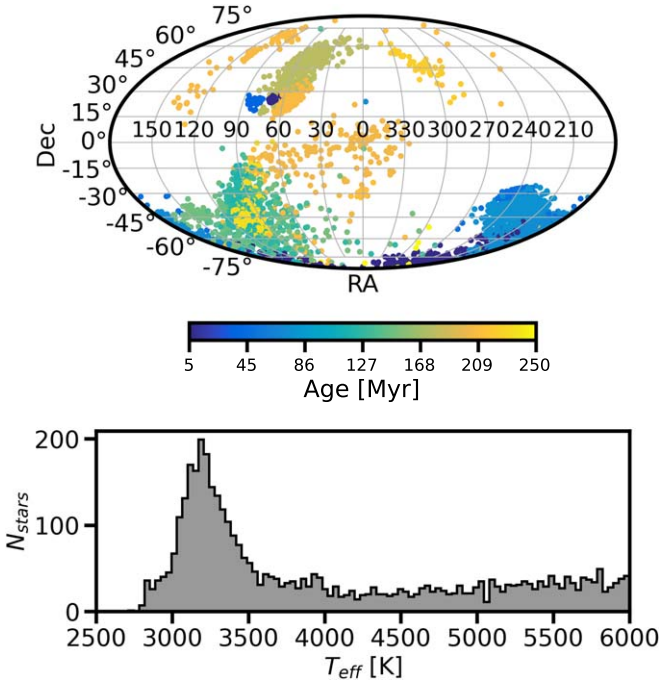

Figure 1. Top: distribution of the selected sample across the sky and colored by the adopted age of the association (see Table 1). The all-sky coverage by TESS has unlocked new populations of stars to observe. We take advantage of this observing strategy to measure flare rates across 26 different nearby young moving groups, clusters, and associations. Bottom: distribution of adopted effective temperatures, $T_{\rm eff}$ [K] for stars in our sample. We include all stars with $T_{\rm eff} \leqslant 6000$ K.

Figure 1, we show the distribution of the on-sky positions, ages, and effective temperatures, $T_{\rm eff}$, of the final sample. Because many of the groups are located at or near the ecliptic poles, many of our targets were observed over multiple TESS sectors. We use $T_{\rm eff}$ as our stellar characterization metric over the standard $M_\star$ because ∼600 stars in our sample lack mass information in the TIC. The entirety of the available data yielded 17,964 light curves processed by the Science Processing Operations Center (SPOC) pipeline (Jenkins et al. 2016), which can be accessed on MAST at 10.17909/t9-nmc8-f686 (MAST Team 2021). Our sample has an average of three light curves per target (although with significant spread across targets). We downloaded all light curves using `lightkurve` (Barentsen et al. 2019). For our analysis, we used the SPOC-processed SAP_FLUX.

2.3. Flare Identification

Once we downloaded the light curves for each target, we performed the following procedure to identify stellar flares. We implemented the machine-learning flare-identification methods presented and described in Feinstein et al. (2020b). This method relies on the similar time-dependent morphologies of all flare events. These flare profiles can generally be described as a sharp rise followed by an exponential decay in the white-light curve. This identification technique implements the convolutional neural network (CNN) `stella` (Feinstein et al. 2020b), although other architectures have been explored for flare identification (e.g., Vida & Roettenbacher 2018). The CNN was trained on a by-eye validated catalog of flares from TESS Sectors 1 and 2 with 2 minute data (Günther et al. 2020).

Table 1
Adopted Ages of Each Young Stellar Population and Number of Stars per Group, $N_{\rm stars}$

Population	Age (Myr)	$N_{\rm stars}$	References
AB Doradus	133^{+15}_{-20}	88	(1)
Blanco 1	$137.1^{+7.0}_{-33}$	428	(2)
Carina	45 ± 9	94	(3)
Carina-Musca	32	35	(4)
Chamaeleon	5	424	(5)
Columba	42	126	(3)
Greater Taurus Subgroup 5	8.5	56	(4)
Greater Taurus Subgroup 8	4.5	122	(4)
Lower Centaurus Crux	15	761	(6)
MELANGE-1	250^{+50}_{-70}	19	(7)
Octans	35 ± 5	64	(8)
Pisces Eridanis	120	219	(9)
Pleiades	$127.4^{+6.3}_{-10}$	1421	(2)
α Persei	$79^{+1.5}_{-2.3}$	625	(2)
IC 2602 system	$52.5^{+2.2}_{-3.7}$	160	(2)
NGC 2451A	48.5	59	(4)
Oh 59	162.2	62	(10)
Platais 9	50	124	(11)
RSG2	126	145	(12)
Theia 301	195	437	(10)
Theia 95	30.2	230	(10)
TW Hydrae	10	24	(3)
Upper Centaurus Lupus	16 ± 2	696	(6)
Upper Scorpius	10	106	(6)
Vela-CG4	33.7	299	(4)
Total		6824	

Note. Age references: (1) Gagné et al. (2018a); (2) Galindo-Guil et al. (2022); (3) Bell et al. (2015); (4) Kerr et al. (2021); (5) Luhman (2007); (6) Pecaut & Mamajek (2016); (7) Tofflemire et al. (2021); (8) Murphy & Lawson (2015); (9) Curtis et al. (2019); (10) Kounkel et al. (2020); (11) Tarricq et al. (2021); (12) Röser et al. (2016).

There are several benefits to using the CNN for stellar flare identification. Primarily, the CNN is insensitive to the stellar baseline flux because it is trained to search *only* based on flare morphology. It is therefore relatively insensitive to the absolute flux levels, so long as the inherent noise does not overwhelm the signal itself. An additional benefit is that rotational modulation peaks—which are themselves driven by stellar heterogeneities—are not accidentally identified as flares. This holds true for stars with rotation periods, $P_{\rm rot} > 1$ day. This is especially advantageous for our sample of young stars, which readily exhibit rotational modulation in their light curves.

Based on these advantages, the final compiled sample of flares is unbiased toward low-amplitude/low-energy flares. It is important to note that these low-energy events are typically not identified in traditional sigma-outlier identification methods (e.g., Chang et al. 2015; Vasilyev et al. 2022). While significant developments have been achieved to better model and detrend stellar variability (e.g., Bicz et al. 2022), these methods can be computationally intensive The `stella` CNN models calculate the probability that a data point in a light curve is associated with a flaring event. Specifically, it takes the light curve (time, flux, flux error) as an input and returns an array with values of [0, 1], which are treated as the probability a data point is (1) or is not (0) part of a flare. We ran every light curve through 10 independent `stella` models and averaged the outputs to ensure that our statistics were accurate. We note that in this

processing, the CNN ignores 200 minutes before and after any gaps in the data. Therefore, any flares which occur during these times are not identified. From by-eye vetting of ∼300 light curves, we found two flares within the first 200 minutes of the orbital gaps. Therefore, we estimate ⩽120 flares are missed in our catalog.

The `stella` code groups individual points with the predictions per data point when identifying a single flare event. We modified this stage of identification slightly from the original flare-identification method. Specifically, we identified all data points with a probability of being associated with a flare of $P > 0.75$. Any data points that were within four cadences of each other were considered to be a single flare event. We did not consider any potential flares that had three or fewer points with $P > 0.75$. This method rejects single-point outliers which can be assigned high probabilities of being flares. We assigned the probability of the whole flare event as the probability of the peak data point.

2.4. Modeling Flare Properties

Flares are well-described in light curves as a sudden increase in flux followed by an exponential decay. We used the analytic flare model, Llamaradas Estelares, which was presented in Tovar Mendoza et al. (2022),[12] to fit and extract parameters of flares in all of the light curves of our sample. This model builds upon the model presented in Davenport et al. (2014). Specifically, it includes the convolution of a Gaussian with a double exponential model in the flare profile.

The analytic model robustly accounts for physically motivated flare features. Specifically, it can incorporate the flare (i) amplitude, (ii) heating timescale, (iii) rapid cooling phase timescale, and (iv) slow cooling phase timescale. We implemented a nonlinear least squares optimization to fit the flare peak time ($t_{\rm peak}$), FWHM, and the amplitude (A) of each flare in the sample. We note that there are several other physically motivated flare models that could be used, such as those presented in Gryciuk et al. (2017), Pietras et al. (2022), and Yang et al. (2023a); these models include using two profiles to fit the impulsive and late phases of the flare. We combine the model with a second-order polynomial fit to a 1.2 hr baseline before and after the flare during only the fitting stage. This was implemented in order to account for any slope due to rotational modulation and therefore was particularly relevant for the rapid rotators ($P_{\rm rot} < 2$ days).

We calculated the equivalent duration, ED, of the flare by integrating the quiescent-normalized flare flux with respect to time. We calculate the flare energy, $E_{\rm flare}$, using,

$$E_{\rm flare} = L_\star\, A\ {\rm ED}\ s. \quad (1)$$

In Equation (1), $L_\star$ is the luminosity of the star and s is a scaling factor defined as $s = B_\lambda(T_{\rm eff})/B_\lambda(T_{\rm flare})$, where $B_\lambda(T)$ is the Planck function. We assume that the flare temperature is 9000 K (Hawley & Fisher 1992; Hawley et al. 1995), although recent NUV flare observations suggest this may be an underestimation (Kowalski et al. 2019; Berger et al. 2023; Brasseur et al. 2023).

[12] https://github.com/lupitatovar/Llamaradas-Estelares

2.4.1. Comparison of Flare Models

Tovar Mendoza et al. (2022) demonstrated that the flare model works well for flares with amplitudes ⩾2 (i.e., double the baseline flux). However, other works such as Pietras et al. (2022) have demonstrated that a double-flare profile better fits high-energy flares. To quantify how well the Llamaradas Estelares model works, we refit and calculate the χ^2 for a subset of high-amplitude flares ($A \geqslant 0.4$) using Equation (3) in Pietras et al. (2022), a double-peak flare model, which is:

$$f(\tau) = \int_0^\tau \left(A_1 \exp\left[\frac{-(t-B_1)^2}{C_1^2}\right] \exp\left[\frac{(t-\tau)}{D_1}\right] + A_2 \exp\left[\frac{-(t-B_2)^2}{C_2^2}\right] \exp\left[\frac{(t-\tau)}{D_2}\right] \right) dt, \quad (2)$$

where A is related to the amplitude of the flare, B relates to the total energy released during the flare, C relates to the timescale of the flare, D is related to the decay timescale, τ is the time of a given cadence, and t is the time to integrate over. The subscripts 1 and 2 indicate which flare variables are associated with the first and second flare profile. We refit 900 high-amplitude flares following Equation (2). We plot the results of this refitting in Figure 2.

Broadly, we find the flare model from Tovar Mendoza et al. (2022) and Pietras et al. (2022) to fit the majority of the high-amplitude flares equally as well (Figure 2(A)). We highlight several examples where one model fits better than the other in Figures 2(B)–(E), and cases where both profiles fit the data equally as well in Figures 2(F)–(G). Flares that prefer the Llamaradas Estelares model tend to have a more accurately fit flare amplitude. Flares that prefer the double-peak model tend to have an extended decay timescale, which is better fit by the addition of a secondary flare. Flares that are fit equally well by both models tend to have a better fit to the amplitude in the Llamaradas Estelares model, but a better fit to the decay timescale in the double-peak flare model.

2.5. Flare Quality Checks

The `stella` CNNs were trained on data from TESS Sectors 1 and 2. However, the noise properties are variable across sectors in TESS data. The CNNs are therefore unable to accurately account for and capture this variation when operating in different sectors. Moreover, the original CNNs were only trained on a sample of 1228 stars. This training sample does not necessarily encapsulate a sufficient distribution of variable star types, such as eclipsing binaries, RR Lyraes, and fast rotators with $P_{\rm rot} < 1$ day (Lawson et al. 2019), which results in the CNNs not being able to properly distinguish these temporal features from flares. We therefore apply additional quality checks to ensure our flare sample has little to no contamination from other sources.

Specifically, we removed flares from our sample that did not satisfy one or more of the following criteria:

1. The amplitude of the flare must be >0.01, the same limits set by Feinstein et al. (2020b).
2. The flare amplitude must be at least twice the standard deviation of the light curve 30 minutes before and 45 minutes after the flare. This ensures that the feature is not a sharp noise artifact.

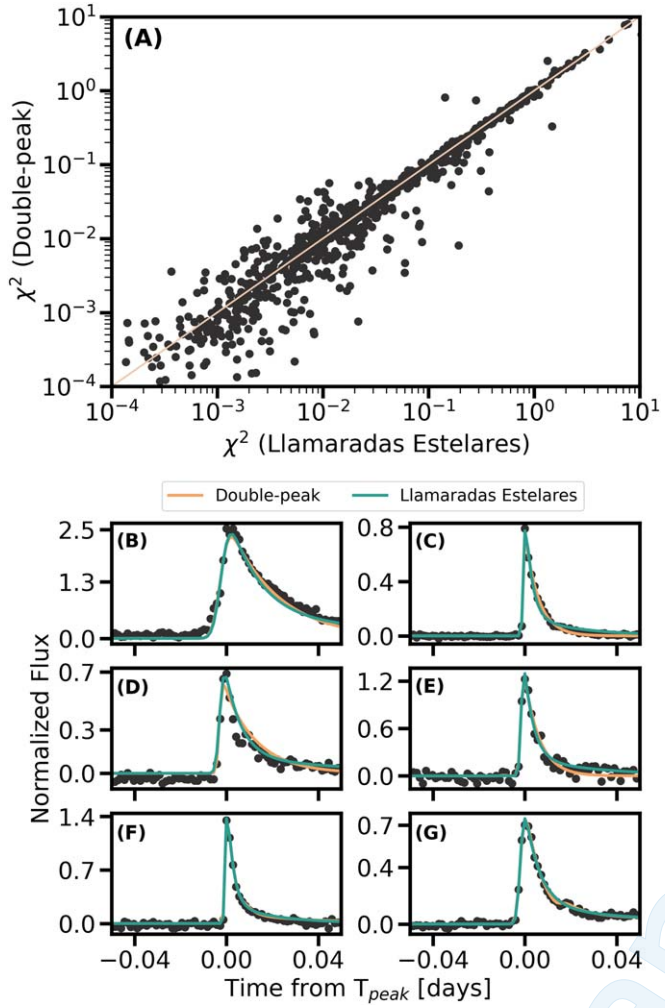

Figure 2. Comparison fits between the Llamaradas Estelares single-peak model from Tovar Mendoza et al. (2022) and the double-peak flare model from Pietras et al. (2022) for flares with $A \geqslant 0.4$. Top (A): comparison in the χ^2 between the best-fit model for 900 flares. A one-to-one line is plotted in peach to guide the eye. Across this sample of high-amplitude flares, there is good agreement between the fits for these two distinct models. Bottom: comparison in best-fit models for a subset of flares. The best-fit Llamaradas Estelares model is plotted in blue; the best-fit double-peak model is plotted in orange. We highlight examples where the double-peak flare model has the better fit (B), (C), the Llamaradas Estelares flare model has the better fit (D), (E), and where the models perform equally as well (F), (G). We note that there is no correlation between the flare amplitude and the preferred model.

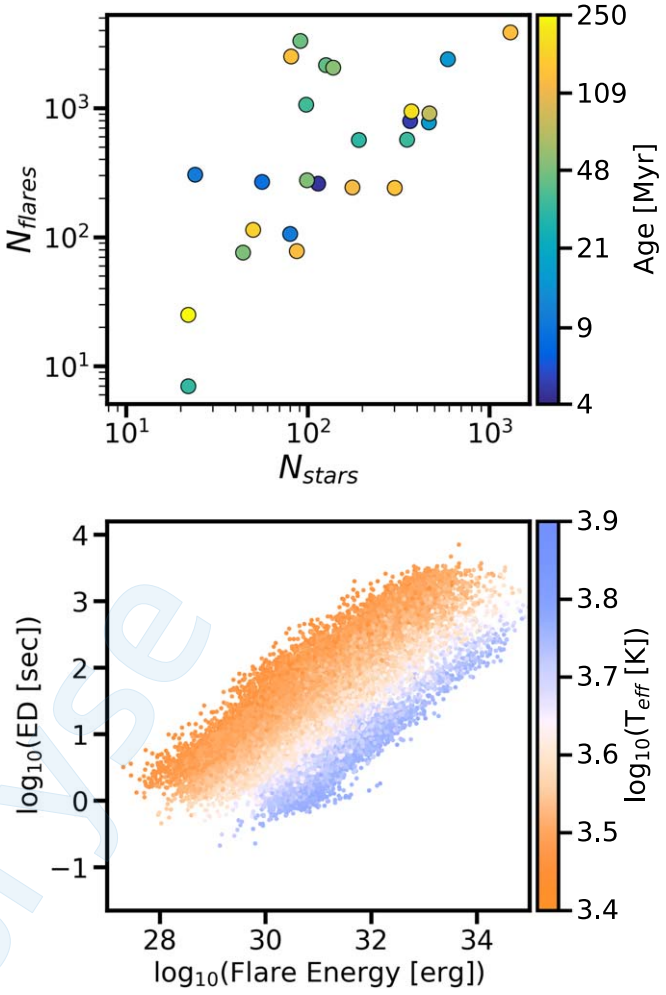

Figure 3. High-level summary of the demographics of flares in our sample. Top: the number of flares identified compared to the number of stars in each nearby young moving group, cluster, or association. A linear relationship is expected. Bottom: distribution of measured TESS energies and equivalent durations of flares in our sample, colored by the probability of the flare as identified with `stella`.

3. The fitted flare model parameters must be physically motivated: FWHM > 0; $A > 0$; ED > 0.
4. The flare parameters must be $\sigma_A < 0.5$ and $\sigma_{t_{peak}} < 0.01$.

We find that flares are often simply mischaracterized noise when the errors on the first and fourth criteria are larger than the cutoffs. These quality checks highlight the need to continuously update machine-learning models, especially when looking at data with varying instrumental systematics.

As a final check, we performed an exhaustive by-eye verification of flares from light curves for stars with flare rates, $\mathcal{R} > 1\,\mathrm{day}^{-1}$. These stars generally tend to have $T_{\rm eff} > 5000$ K and TESS magnitudes <8. Therefore, their light curves are dominated by sharp noise, which `stella` often mischaracterizes as flares. As a final cut, the sample only includes events that have a probability $P \geqslant 98\%$ of being a true flare. After performing these additional checks, we obtain a robust final flare sample of 26,355 flares originating from 3160 stars (Figure 3).

2.6. Measuring Rotation Periods

In addition to understanding flare statistics across young stars, we measure the rotation periods, $P_{\rm rot}$, of stars in our sample. We then search for correlations between $P_{\rm rot}$ and Rossby number, R_0. Seligman et al. (2022) demonstrated that stars with low Rossby numbers $R_0 < 0.13$ exhibit shallower FFD slopes. These shallower slopes are caused by an excess of high-energy flares compared to lower-energy flares.

In order to perform this, we describe how we measure stellar rotation periods from the TESS light curves. To this end, we used `michael`,[13] an open-source Python package that robustly measures $P_{\rm rot}$ using a combination of traditional Lomb–Scargle periodograms and wavelet transformations. `michael` measures $P_{\rm rot}$ using the `eleanor` package, which extracts light curves from the TESS Full-Frame Images (FFIs; Feinstein et al. 2019).

[13] https://github.com/ojhall94/michael

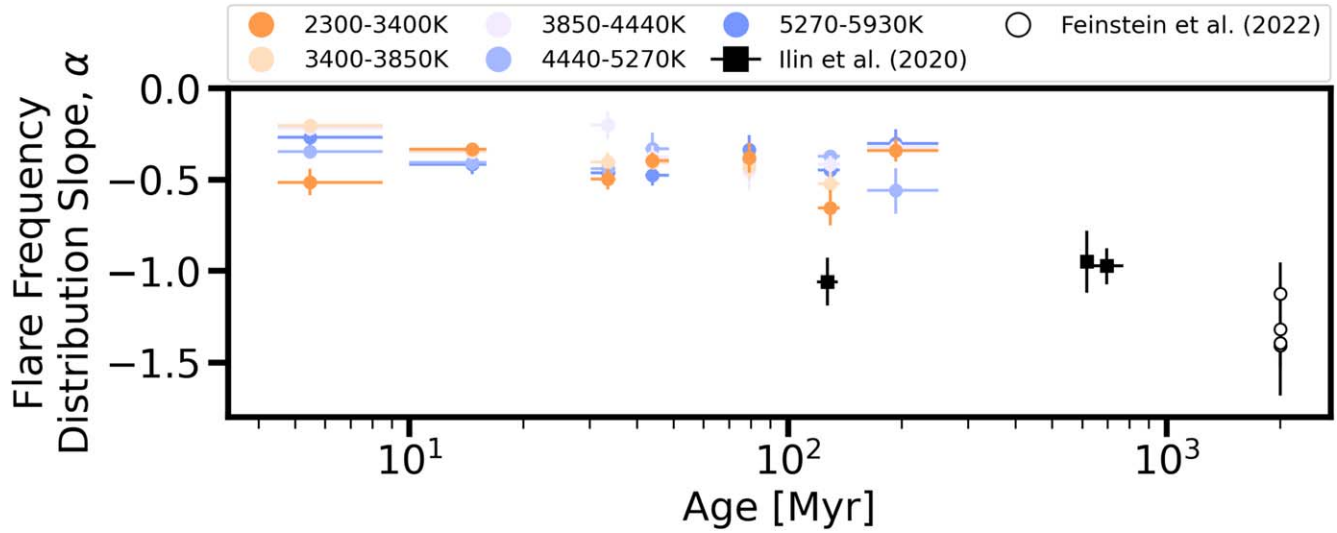

Figure 4. Measured flare frequency distribution slopes, α, as a function of the stellar effective temperature, $T_{\rm eff}$, and age. We measured these FFDs with respect to flare energy. We find that the FFD slopes as a function of the energy are consistent with $\alpha = -0.6$ to -0.2 for stars <300 Myr in TESS observations. A shallower FFD slope is indicative of more high-energy flares. We present all measured FFDs in the Appendix and all measured slopes and errors in Table A1. We find the shallowest slopes for stars $T_{\rm eff} = 3400$–4440 K, with a range from $\alpha = -0.44$ to -0.22. We do not include the results for stars $T_{\rm eff} = 3850$–4440 K and $t_{\rm age} = 20$–40 Myr as this bin contained only six stars with detected flares. We present the average results of measured FFD slopes for the Hyades, Pleiades, and Praesepe clusters from Ilin et al. (2021) as black squares. We present the results of measured FFD slopes for all TESS primary mission targets in white circles (Feinstein et al. 2022b) as "field-age." We discuss what drives the difference between our sample and Ilin et al. (2021) in Section 3.1.

We ran `michael` on all stars in our samples from which flares were identified. The estimated rotational periods were subsequently vetted by eye with the `michael` diagnostic plots. This vetting was implemented to ensure that the measured $P_{\rm rot}$ was not a harmonic of the true $P_{\rm rot}$ or from an occulting companion. This led to robust measurements of rotation periods for 1847 stars in total. Additionally, we identified 17 eclipsing binaries or potentially new planet candidates.

3. Flare Rates of Young Stars

In this section, we use the previously described methodology to estimate the flare rates of the young stars in our sample. We implement three main steps in this analysis. First, we perform the standard FFD fitting of a power law to the distribution of flare energies described in Section 3.1. Next, we fit the relationship between R_0 and flare rates in Section 3.2. Finally, we fit a truncated power law to the distribution of flare amplitudes in Section 3.3 to identify correlations between R_0 and flare distributions.

The number of stars and flares in each association varied greatly (Figure 3). This was primarily caused by the limited number of stars that had been observed at 2 minute cadence in TESS. We therefore did not measure FFD properties as a function of the association. Instead, we group stars by $T_{\rm eff}$ and average adopted association age.

We define the following spectral-type bins by $T_{\rm eff}$:

1. M stars below the fully convective boundary ($T_{\rm eff} = 2300$–3400 K),
2. early-type M stars ($T_{\rm eff} = 3400$–3850 K),
3. late K stars ($T_{\rm eff} = 3850$–4440 K),
4. early K stars ($T_{\rm eff} = 4440$–5270 K),
5. G stars ($T_{\rm eff} = 5270$–5930 K).

We did not include any stars hotter than $T_{\rm eff} > 5930$ K. These hot stars generally exhibit light curves dominated by noise in the TESS observations. Additionally, we grouped stars in the following age space: 4–10 Myr (including Upper Scorpius and TW Hydrae), 10–20 Myr, 20–40 Myr, 40–50 Myr, 70–80 Myr, 120–150 Myr, and 150–300 Myr. We note that there is a gap in age from 50 to 70 Myr, which could be expanded with the identification of more associations in this age range.

3.1. Standard Power-law Fits

We fit the stars' FFD slopes, approximated as a power law, using the $T_{\rm eff}$ and age bins described above. Flares were binned into 25 bins in log space from 10^{27} to 10^{35} erg. The FFD has a notable turnover energy, $E_{\rm turnover}$, when our detection method is incomplete due to the low amplitude of those flares. The FFD slope is often fit to flares with energies $E \geqslant E_{\rm turnover}$. We perform our fits following the same methodology. This turnover in the FFD cannot be accurately modeled with a power law. We present our FFDs as a function of $T_{\rm eff}$ and age in Figure A1; points that were fit to measure the FFD slope are presented in black, while the full FFD is presented in gray. We present our best-fit results in Table A1.

We fit the FFD using the Markov Chain Monte Carlo (MCMC) method implemented in `emcee` (Goodman & Weare 2010; Foreman-Mackey et al. 2013). Specifically, we fit for the slope, α, y-intercept, b, and an additional noise term, f. This noise term accounts for an underestimation of the errors in each bin. We initialized the MCMC fit with 300 walkers and ran our fit over 5000 steps. We discarded the first 100 steps upon visual inspection, after which the steps were fully burned in. The measured FFD slopes, α, are presented in Figure 4. We approximate the error on the slope as the lower 16th and upper 84th percentiles from the MCMC fit.

Overall, we measure a shallower FFD for stars of all masses at $t_{\rm age} < 300$ Myr. A shallower FFD indicates there are more high-energy flares. The measured FFD slopes are shallower than those measured using smaller samples of young stars. Jackman et al. (2021) fit the three FFDs for M3–M5, M0–M2,

and K5–K8 stars younger than 40 Myr that had been observed with the Next Generation Transit Survey. They measured slopes of 0.94 ± 0.04, 0.69 ± 0.05, 0.82 ± 0.14 per bin, which each contained $\leqslant$120 flares. It is also worth noting that the slopes measured here are based on up to an order of magnitude more flares per fit. Our sample also has a longer temporal baseline, allowing for the occurrence of more high-energy flares. Accumulating more high-energy flares in the FFD, if such events occur, will result in a shallower FFD slope. TESS flare statistics for main-sequence stars have indicated steeper FFDs (Feinstein et al. 2022b). Therefore, the FFDs presented here are not strictly impacted by longer observations but are the result of more high-energy flares on young stars.

There is a 1–3σ discrepancy between the FFD slope measured in Ilin et al. (2021) and the work presented here at ages $\sim$120 Myr (α ranges from -1.32 ± 0.19 to -0.91 ± 0.18, depending on the $T_{\rm eff}$ bin). Ilin et al. (2021) used the K2 30 minute light curves for their analysis, compared with our TESS 2 minute light curves. Additionally, our sample has $\sim$2$\times$ the number of stars and $\sim$7$\times$ the number of flares as in Ilin et al. (2021). First, we test if these discrepancies are driven by differences in sample binning. We reevaluate the FFDs assuming the $T_{\rm eff}$ bins presented in Table 3 of Ilin et al. (2021). We find α remains consistent with our presented values to within $\sim$1σ of the nearest temperature bin. Second, we reevaluate the FFDs assuming the total number of flares fit in Ilin et al. (2021). We draw $n_{\rm fit}$ (last column in Table 3 of Ilin et al. 2021) flares from our sample 100 times without replacement, refit the FFD, and take the average FFD slope from that subsample of flares to our results. We find α remains consistent with our presented values to $\sim$2σ. We note that in most cases $n_{\rm fit,Ilin\ et\ al.\ (2021)} < n_{\rm fit,this\ work}$. Therefore, the increased disagreement in α could be due to smaller sample sizes.

Additionally, we test if the difference in α is driven by the cadence differences between K2 (30 minutes) and TESS (2 minutes). We bin all of the flares in our sample down to a 30 minute cadence, refit for flare A and ED, and recalculate the flare energy. We refit the FFD for this altered sample and measure FFD slopes consistent with $\sim$1σ with those presented in this work. Therefore, the discrepancy seen here is not driven by observational differences between K2 and TESS.

Finally, we test if the differences are driven by the range of energies that are fit. The CNN-based flare-detection algorithm has previously been demonstrated to be less biased against lower-energy flares. Like this work, Ilin et al. (2021) fit the FFD across flare energies that are not affected by a reduced efficiency in the low-energy flare detection, $E \geqslant E_{\rm turnover}$. In energy space, these fits begin between $E_f = 10^{32-33}$ erg, compared to our fits which begin between $E_f = 10^{31-32}$ erg (Appendix). When we limit our sample to $E_f \geqslant 10^{32.5}$ erg, we find the FFD slopes become *steeper* and more consistent with the values of α presented in Ilin et al. (2021). Therefore, the difference in α between this work and Ilin et al. (2021) for stars with $t_{\rm age} = 120$–150 Myr is driven by the lower-energy flares, with which we are more complete with TESS than K2.

3.2. Flare Rate Dependence on Rossby Number

The Rossby number, R_0, is a parameter that incorporates several properties that are known to affect the stellar dynamo, such as the rotation period and stellar mass. In the context of stellar dynamo the Rossby number indicates the dominance of the convective versus rotational dynamo. It is defined as $R_0 = P_{\rm rot}/\tau$, where τ is the convective turnover time. We convert our measured rotation periods to R_0, approximating τ following the prescription in Wright et al. (2011). We equate the flare rates, $\mathcal{R}$, for individual stars as

$$\mathcal{R} = \frac{1}{t_{\rm obs}}\left(\sum_{i=1}^{N} p_i\right). \tag{3}$$

In Equation (3), $\mathcal{R}$ is the flare rate in units of day^{-1}, $t_{\rm obs}$ is the total amount of time a target was observed with TESS, and p_i is the probability that flare i is a true flare as assigned by `stella`. We compare the calculated R_0 to measured flare rates for all stars with measured $P_{\rm rot}$. The results are presented in Figure 5.

From these results, we are able to evaluate the dependence of the flare rate on age, spectral type, and R_0. We split the sample between stars younger and older than 50 Myr. This age roughly correlates to the age at which GKM stars turn onto the main sequence. The flare rate of stars younger than 50 Myr slightly decreases with increasing R_0. However, there is a significant amount of scatter in this relationship.

As can be seen by comparing the upper and lower panels in Figure 5, the flare rate dependence on the Rossby number is most evident in older, more massive stars between 50 and 250 Myr. There is minimal evolution in both the average flare rate and R_0 between the two samples for M stars. For K stars, R_0 evolves more dramatically during the first 250 Myr while the scatter in the flare rate decreases. For G stars, the scatter in R_0 decreases and the average flare rate across the sample decreases. We present a compiled histogram for all stars in our sample in the right column of Figure 5.

To better understand this trend for the GKM sample, we fit three functions to the flare rate Rossby number parameter space: (i) a constant value, (ii) a single power law, and (iii) a piecewise function consisting of a constant value and a power law. We computed the χ^2 between each of these fits and the data. For (iii), we fit for where the R_0 turnover should occur by computing the χ^2 across a range of $R_0 = [0.09, 0.18]$. We weighted the data points based on the density of points in a given bin (Figure 5). For 4.5–50 Myr old stars, the distribution is best fit with a single power law with slope $m = -0.102 \pm 0.018$ and y-intercept $b = -0.660 \pm 0.017$. For stars 50–250 Myr, the distribution is best fit with a piecewise function of the form:

$$\mathcal{R} = \begin{cases} C & R_0 \leqslant 0.136 \\ 10^{b} * R_0^{m} & R_0 > 0.136. \end{cases} \tag{4}$$

In Equation (4), $\mathcal{R}$ is the flare rate, $C = 0.269 \pm 0.007$, $m = -0.612 \pm 0.039$, and $b = -1.113 \pm 0.035$. The location of the turnover is consistent with what has been measured in other observations of magnetic saturation for partially and fully convective stars (e.g., $L_{\rm X}/L_{\rm bol}$; Wright et al. 2018).

With a sample of 851,168 flares detected in both Kepler 1 and 30 minute cadence data, Davenport (2016) searched for a relationship between Rossby number and relative flare luminosity. This work determined that the relationship could be fit by a broken power law, with a break at $R_0 = 0.03$ and a slope of $m \sim -1$ dominating higher R_0. However, a single power law is slightly preferred over the broken power law. While the metrics used between Davenport (2016) and this paper are different, both suggest a saturation in flares for stars with low R_0. Additionally,

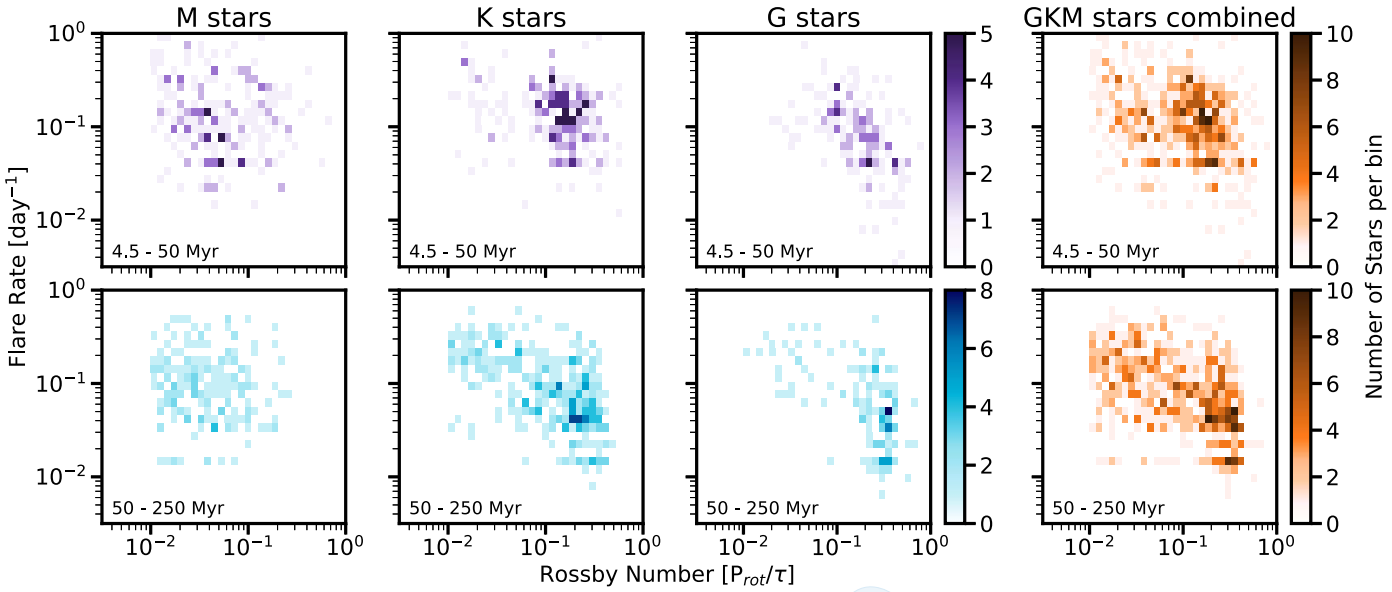

Figure 5. Comparison of Rossby Number, R_0, and flare rate for young GKM stars. For the younger sample (top row; $t_{age} = 4.5$–50 Myr), we find no correlations between flare rate and R_0. For the slightly older sample (bottom row; $t_{age} = 50$–250 Myr), we find no change in the average flare rate for M stars. For K and G stars, we start to see some evolution in this relationship. For K and G stars, we see that as R_0 increases, the average flare rate decreases. This could indicate that as stars spin down, their flare activity also begins to decline. We find that for the full GKM sample of stars (bottom row, rightmost column), the relationship between R_0 and flare rate is best fit by a broken power law, with a turnover at $R_0 = 0.136$. For the younger full sample (top row, rightmost column), we find this relationship is best fit by a single power law. The histograms are colored by number of stars in each bin.

Medina et al. (2020) found a broken-power-law relationship between R_0 and the flare rate for flares with $E_f > 3.16 \times 10^{31}$ erg, corresponding to the completeness threshold of their sample. Medina et al. (2020) analyzed light curves of 419 low-mass ($M_\star = 0.1$–$0.3 M_\odot$) main-sequence stars in the solar neighborhood observed by TESS. They found that the flare rate saturates at $\log(\mathcal{R}) = -1.30 \pm -0.08$ for $R_0 < 0.1$ and rapidly declines for $R_0 > 0.1$. Yang et al. (2023b) analyzed 7082 stars with measured $P_{\rm rot}$ observed during TESS sectors 1–30 and found a broken power law described the relationship between $\Delta\text{Flare}/L_\star$ for M dwarfs, with a break between $R_0 = 0.1$–0.13, which is consistent with this work. While there are differences in sample selection between our work and previous studies, all are consistent with flare rate saturation for stars with low R_0 and a steep drop-off in flare rate for stars with higher $R_0 > 0.1$.

3.3. Truncated Power-law Fits

We search for evidence of variations of the FFDs as a function of the flare amplitude versus Rossby number, R_0. This is motivated by the data presented in Seligman et al. (2022). In that work, they modeled flares driven by magnetic reconnection events driven by rotational forces as well as convective dynamo. Seligman et al. (2022) found that stars with $R_0 < 0.13$ exhibited shallower FFD slopes than stars with $R_0 \geqslant 0.13$ to several sigma significance. The differences in the FFDs were indicative of relatively more high-energy flares than low-energy flares. This was interpreted as evidence of a more dominant rotational dynamo compared to the convective dynamo, which preferentially produced longer magnetic braids in the stellar coronae.

In this subsection, we test this theory with a much larger sample of stars (1847 instead of 807 stars). We fit the distributions separated by the fitted R_0 presented in Section 3.2. In order to perform the fits, we follow the prescription described in greater detail in Seligman et al. (2022). Here, we provide a brief summary of the prescription. Specifically, we fit a truncated power-law distribution of the form,

$$dp/dA \propto A^{-\alpha_T} e^{-A/A_*}. \quad (5)$$

In Equation (5), A is the amplitude of the flare, A_* is a flare amplitude cutoff parameter and α_T is the slope, rather than α. We fit the slopes using the MCMC method implemented in `emcee` (Goodman & Weare 2010; Foreman-Mackey et al. 2013). We used the log-likelihood function in Seligman et al. (2022) and fit for A_* and α_T. We initialized the MCMC fit with 200 walkers and evaluated the fit over 5000 steps. The first 1000 steps were discarded upon visual inspection. The results are presented in Figure 6.

We find that stars with $R_0 \leqslant 0.136$ have a best-fit slope of $\alpha_T = 1.076 \pm 0.020$, while stars with larger R_0 have a best-fit slope of $\alpha_T = 1.604 \pm 0.040$. This result agrees with the results presented in Seligman et al. (2022). This is not the first instance we have seen a correlation in FFDs as a function of R_0. Candelaresi et al. (2014) noted that faster-rotating stars have higher superflare rates derived from Kepler data. The spectroscopic survey presented in Notsu et al. (2019) found that the maximum flare energy decreased as $P_{\rm rot}$, and consequently R_0, increased. Mondrik et al. (2019) identified flares across 2226 stars observed with MEarth and found an increase in the flare rate between stars with low $R_0 < 0.04$ and stars with intermediate $R_0 = (0.04, 0.44)$, and a subsequent decrease in the flare rate for stars with high $R_0 > 0.44$. While our bins of stars by R_0 are not as fine as those presented in Mondrik et al. (2019), the correlation in ΔR_0 remains consistent.

4. Evidence for Stellar Cycles from Variable Flare Activity

The Sun undergoes an 11 yr solar cycle during which it oscillates between high and low magnetic activity. This magnetic cycle manifests in a variety of observables. One of the primary indicators of the solar cycle is a stark change in the

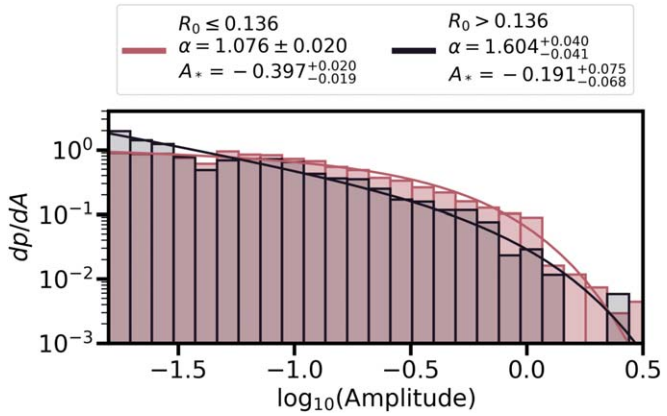

Figure 6. Flare frequency distributions, as a function of the flare amplitude, for stars with $R_0 \leqslant 0.12$ (red) and stars with $R_0 > 0.12$ (black). We present the best-fit model and the best-fit values of the model slope and normalization factor in the legends. Our sample of $R_0 \leqslant 0.12$ includes 13,132 flares from 800 stars; our sample of $R_0 > 0.12$ includes 5603 flares from 747 stars. We find the stars with smaller Rossby numbers have shallower slopes, consistent with more, high-energy flares and a more dominant rotational dynamo (Seligman et al. 2022).

flare rate; this rate can vary by more than an order of magnitude between Solar maxima and minima (Webb & Howard 1994). Moreover, the energetics of the flares that are produced on the solar surface vary dramatically over the course of the solar cycle (Bai & Sturrock 1987; Bai 2003). Direct and indirect evidence of the solar cycle has also been observed in radio flux, total solar irradiance, the magnitude and geometry of the magnetic field, coronal mass ejections affiliated with flares, geomagnetic activity, cosmic ray fluxes, and radioisotopes in ice cores and tree rings. For a recent review, see Hathaway (2015).

While other stars should also experience activity cycles like the Sun, they are more difficult to measure. Constraints on stellar cycles have predominantly relied on long-baseline variations in stellar photometry, typically observed at cadences that cannot resolve stellar flares (see recent reviews by Işık et al. 2023; Jeffers et al. 2023). However, tracing stellar cycles via stellar flares may be more reliable, as flares are a direct consequence of magnetic activity. Scoggins et al. (2019) explored measuring the stellar cycle length of KIC 8507979, a star in the Kepler field that was observed for 18 90 day quarters. Scoggins et al. (2019) found the flare rate decreased over each quarter, which could be fit by $L_{\rm fl}/L_{\rm Kp} = (-9.96 \pm 3.94) \times 10^{-2} \times t_{\rm yr} + (2.43 \pm 0.11)$, where $t_{\rm yr}$ is the time in years, and $L_{\rm fl}/L_{\rm Kp}$ is a parameterization of the Kepler flare rate (Lurie et al. 2015).

4.1. Flare Observables from the Sun

Here, we explore observables from solar flares between 2002 and 2018 in the Reuven Ramaty High Energy Solar Spectroscopic Imager (RHESSI; Lin et al. 2002) flare catalog.[14] The RHESSI mission observes the Sun across a wide range of X-ray energies, from 3 keV to 17 MeV, with high temporal and energy resolutions as well as high signal sensitivity. Such a wide energy range enables the ability to explore both the thermal and nonthermal emission observed during flare events. Over 16 yr of operations, over 100,000 solar flares have been observed and characterized in RHESSI data. These observations covered the second half of Solar Cycle 23 and the beginning of Solar Cycle 24. We use the publicly available RHESSI flare catalog to determine metrics that would be most useful when searching for evidence of stellar cycles. One potential issue with this analysis is that the hard X-ray (HXR) observations from RHESSI and white-light observations from TESS may not be directly correlated. However, there is a close spatial and temporal correspondence between HXR and white-light flares on the Sun (Fletcher et al. 2007; Krucker et al. 2011; Kleint et al. 2016). In particular, Namekata et al. (2017) demonstrated the difference in spatially resolved flares as observed with RHESSI HXR and the Solar Dynamics Observatory/Helioseismic and Magnetic Imager (HMI) white light. In some examples, the HMI white-light emission is seen to last longer than the HXR, indicating the white-light emission is related to nonthermal electrons.

However, other examples of simultaneous HXR and white-light flare observations in Namekata et al. (2017) show similar flare durations. Therefore, we take the HXR solar flares with energies between 25 and 50 keV as likely representative of solar white-light flares and are a comparable sample to our TESS sample. First, the total number of flares detected in the 25–50 keV bandpass varied by 650 flares from the solar maximum in 2002 to the solar minimum in 2008. This variation correlates to a change in flare rate from 1.81 to 0.02 flares day^{-1} on average. Second, the FFD changes between solar minimum and maximum because the frequency of the highest-energy flares decreases. Finally, the total flare luminosity relative to the total luminosity correlates with the stellar cycle. This is defined by Lurie et al. (2015) as

$$\frac{L_{\rm flare}}{L_\star} \equiv \frac{\xi_{\rm flare}}{t_{\rm exp}}, \tag{6}$$

where $L_{\rm flare}$ is the total luminosity emitted by flares, $L_\star$ is the luminosity of the star, $\xi_{\rm flare}$ is the sum of the equivalent duration of all flares observed, and $t_{\rm exp}$ is the exposure time of the observations. These results for the Sun are presented in the leftmost column of Figure 7.

4.2. Quantifying Flare Activity Over 5 yr of TESS Observations

The TESS Extended Missions have provided a five-year baseline that we can use to search for evidence of stellar cycles. This is a comparable baseline to Kepler, although with sparser sampling. We search for evidence of stellar cycles within our sample of fast rotators. Our sample contains 108 stars that have been observed for $t_{\rm obs} \geqslant 200$ days across five years. We search for evidence of changes in the stellar magnetic activity by looking for correlations in (i) variations in the total luminosity emitted in flares (ii) the total flare rate per year and (iii) annual changes in the FFD. We group our observations by the year in which the observations were taken, even for the cases where the star was not continuously observed throughout that year (e.g., Sectors 1–26 are Year 1, Sectors 27–55 are Year 2, and Sectors 56–67 are Year 3).

We searched our 108 candidates by eye for correlations in the aforementioned criteria. The correlations are categorized into the following four options: (i) Positive: $E_{\rm f,max}$ and the total number of flares has increased over five years; (ii) Negative: $E_{\rm f,max}$ and the total number of flares has decreased over five years; (iii) Trough: $E_{\rm f,max}$ and the total number of flares was greater in the first and third years observed with a minimum in

[14] https://hesperia.gsfc.nasa.gov/rhessi3/data-access/rhessi-data/flare-list/index.html

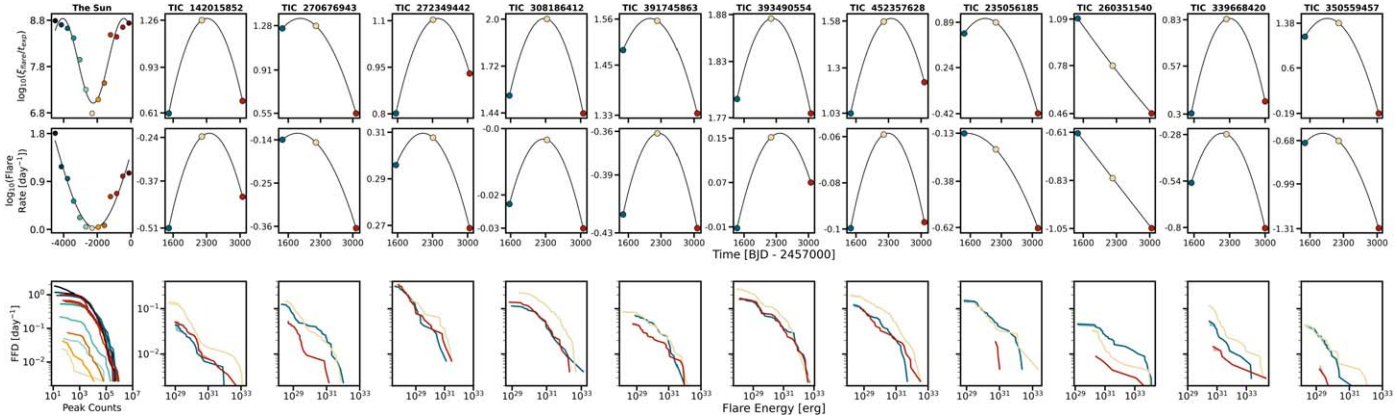

Figure 7. Comparison of three flare-driven metrics in searching for evidence of stellar cycles. Each column contains information for the Sun (left), followed by TIC 142015852, 269797536, 270676943, and 278825715. The top row shows trends in the fractional luminosity emitted in flares, $L_{\rm fl}/L_{\rm TESS} \equiv \xi_{\rm flare}/t_{\rm exp}$ (Lurie et al. 2015). The second and third rows show the calculated flare rate and cumulative FFD, respectively. For the Sun, we used the RHESSI X-ray flare catalog and binned the flares per year from 2002 February to 2014 February. The Sun shows clear trends in $\xi_{\rm flare}/t_{\rm exp}$ and flare rate over the 12 yr solar cycle. The cumulative FFD shows that (i) the overall number of flares decreases, which can be seen in the flare rate as well and (ii) the high-energy flare end of the distribution decreases. A quadratic polynomial is plotted to help guide the eye. It is important to note that these fits do not provide constraints on the length of potential stellar cycles in these stars due to the limited baseline obtained with TESS thus far. We present the measured flare rates and fractional luminosity emitted for each star in Table A2.

the second year; (iv) Peak: $E_{\rm f,max}$ and the total number of flares was fewer in the first and third years observed with a maximum in the second year.

From these three observables, we identified eleven stars which all display evidence of scenario Peak, with the exception of one star displaying evidence of scenario Negative, which is presented in Figure 7. These stars are TIC 142015852, 235056185, 260351540, 270676943, 272349442, 308186412, 339668420, 350559457, 391745863, 393490554, and 452357628. Our sample includes seven early-type M stars, two late K stars, one early K star, and one G star. TIC 272349442 is a candidate member of TW Hydrae ($t_{\rm age} = 10 \pm 3$ Myr), TIC 142015852, 270676943, 308186412, 339668420, 350559457, and 452357628 are candidate members of Carina ($t_{\rm age} = 45 \pm 9$ Myr), TIC 235056185 and 260351540 are candidate members of IC 2602 ($t_{\rm age} = 52.5 \pm 2.95$ Myr), and TIC 391745863 and 393490554 are candidate members of the AB Doradus Moving Group ($t_{\rm age} = 133 \pm 12.5$ Myr).

We report the measured $\xi_{\rm flare}/t_{\rm exp}$ and flare rates across all three years, as presented in Figure 7 in Table A2. Across our sample, we find the largest change in flare parameters in TIC 235056185, which has a $\Delta \log_{10}(\xi_{\rm flare}/t_{\rm exp}) = 1.14$ and $\Delta\mathcal{R} = 0.5$. Additionally, we see some targets (e.g., TIC 350559457) become very flare quiet, going from $\mathcal{R} = 0.2$ day^{-1} to $\mathcal{R} = 0.05$ day^{-1}, which is obvious when visually inspecting the light curve. For stars showing the Peak scenario, we find that the years before and after the peak do not necessarily return to the same value of $\xi_{\rm flare}/t_{\rm exp}$ and $\mathcal{R}$, although it does for some stars.

4.3. Flare Recovery per TESS Year

The majority of stars identified with evidence of stellar cycles exhibit the Peak scenario. To determine if this is astrophysical or driven by some unknown instrumental systematic, we perform an injection-recovery test on this subsample of stars. Injection-recovery tests are used to address biases in our detection method. Injection-recovery tests are typically not recommended for machine-learning detection techniques (Feinstein et al. 2020b). However, we perform them because these are some of the first results of searching for evidence of stellar cycles via flare activity.

We inject a total of 50 flares into each sector of data for our eleven stars. We draw the amplitude of our flares from a Gaussian distribution centered at a 3% increase in flux, with a standard deviation of 1%. We do not inject flares with amplitudes below 0.5%. We used the Llamaradas Estelares flare model. We fit a line between flare amplitude and FWHM from our new catalog to extract an appropriate FHWM for any given amplitude. We added additional noise to the FHWM, as the relationship between amplitude and FWHM exhibits scatter similar to the distribution of flare energy and ED shown in Figure 3. Once the flares were injected, we followed the steps outlined in Sections 2.3–2.5 to identify these injected flares.

We considered a flare recovered if the $t_{\rm peak}$ is within 15 minutes of the injected $t_{\rm peak}$. We are able to recover 93% of flares with $A \geqslant 3\%$ and 80% of flares with $A < 3\%$. This is consistent with previous results using this flare-identification method (Feinstein et al. 2020b). We note that there is a steep drop-off in flare recovery rate at $T_{\rm mag} > 13$, with average recovery rates dropping from 90% to 70%. The variation in recovery rates between years observed by TESS ranges from 1% to 8% across all eleven targets. There is no correlation between recovery rate, $\xi_{\rm flare}/t_{\rm exp}$ and flare rate, with the exception of TIC 142015852 and 339668420. We find an 8% increase between Years 1 and 2 and a 3% decrease between Years 2 and 3 in the recovery rate for TIC 142015852. Additionally, we find a 1% increase between Years 1 and 2 and a 2% decrease between Years 2 and 3 in the recovery rate for TIC 339668420. An 8% change in the recovered flare rate correlates to $\Delta(\xi_{\rm flare}/t_{\rm exp}) = 0.09$, assuming ED = 1 minute, and a $\Delta\mathcal{R} = 0.03$. These estimates are smaller than the annual variations seen in flare statistics for these two stars, leading us to conclude that these variations are astrophysical.

4.4. Observing Peaks in Stellar Flare Activity

In Section 4.3 we demonstrated that 10 out of 108 stars with >200 days of observations exhibited Peak behavior in their variability patterns and found no bias in flare detection as a function of the year. This is approximately what we would

expect to find for an unbiased sample. Our analysis requires a large number of bright flares to be observable to characterize the stellar cycle. Therefore, our sample of objects should be biased toward stars that are undergoing a local maximum, rather than a local minimum, in their activity cycle.

It is not clear what the length of the activity cycles are for stars other than the Sun. For this order of magnitude estimate, we therefore assume that the activity cycles of all stars in our sample are similar to that of the Sun. This approximation is valid if the length of stellar cycles on average is not more than an order of magnitude different than that of the Sun. By observing $N \sim 108$ stars for a $\tau \sim 5$ yr baseline, assuming that each has a $P \sim 10$ yr activity cycle, we would expect that during that time period, $\tau/PN \sim 50$ stars should experience a peak in their stellar cycle during the observations. Moreover, our analysis will only be sensitive to activity cycles if there is not only a peak but also lower activity in the year before and after the peak. Therefore, the number of stars that we would expect to identify that have a peak in Year 2 should be $\tau/PN/3 \sim 16$. Therefore, we would expect to identify $\sim$16 stars exhibiting a peak in their activity cycle during these observations, which is similar to what we have found.

However, it is likely that there is a variety of lengths of stellar cycles in our population and the exact correspondence between the number found and the number estimated is simply a manifestation of the crude order of magnitude approximation that we employed rather than an exact correspondence. Nevertheless, this represents tentative detections of peaks in stellar activity cycles and that on average the length of these cycles is not an order of magnitude different than that of the Sun.

The results presented here are consistent with those presented in previous studies of magnetic activity cycles in young stars. Oláh et al. (2016) analyzed 29 stars from the Mount Wilson survey, which had $\sim$36 yr of Ca II H and K monitoring. Roughly 16 stars in this sample have constrained ages of $<$1 Gyr via gyrochronology. This sample of stars has $P_{\rm rot} = 18.1 \pm 12.2$ days and magnetic activity cycles of $P_{\rm cyc} = 7.6 \pm 4.9$ yr. There is significantly more dispersion in the young stellar cycle lengths than for the older stars. Oláh et al. (2016) concluded that young stars show more complex interannual variations in magnetic activity. While stars age, magnetic braking will increase the rotation of the star. Once this process has occurred, the magnetic activity cycle becomes more well-behaved, as seen in the Sun.

We apply the relationship between $\log(1/P_{\rm rot})$ and $\log(P_{\rm cyc}/P_{\rm rot})$ described in Oláh et al. (2016) to estimate the activity cycles in our sample. 10 of our 11 candidates have measured $P_{\rm rot} = 0.41$–5.22 days. Using the best-fit slope of 0.76 ± 0.15, we estimate the $P_{\rm cyc} = 0.81$–1.49 yr. Strong evidence of shorter activity cycles than $\sim$3 yr may be missed by the sparse annual sampling from TESS. Redesigning the next TESS extended mission to stare at the northern and southern ecliptic poles continuously for two years, instead of alternating poles, may help resolve these shorter activity cycles, if present.

4.5. Validating Stellar Activity Cycles

The stars presented in this work present examples that stellar activity cycles could be identified by characterizing stellar flares and measuring flare rates. In addition to flare rates, it would be beneficial to conduct detailed spectroscopic follow-up of these candidates. For example, detailed monitoring of Ca II H and K lines for these targets could reveal if their activity cycles are similar to that seen from the flare rates. Unfortunately, our candidates are located too far south to have been included in the Mount Wilson HK project, which aimed to understand stellar chromospheric activity on a variety of timescales (Wilson 1968). Monitoring the overall XUV luminosities of these targets could provide additional insights into the variability of the targets. Additionally, more continuous time-series photometry of these targets would provide more stringent constraints on the flare variability for these targets. While long time-series photometry, such as that achieved with TESS and Kepler are ideal, more sparse but consistent photometric monitoring for stellar flares may provide useful additional supplemental data to TESS observations. This is especially true for the times when TESS is observing in the opposite ecliptic hemisphere.

The TESS FFIs allow for the creation of light curves for objects in $\sim$95% of the sky (e.g., Feinstein et al. 2019). During its primary mission (2018 July–2020 July), the TESS FFIs were taken every 30 minutes. During its first extended mission (2020 July–2022 September), the FFI cadence was decreased to 10 minutes. Now, during its second extended mission (2022 September–2025 September), the FFI cadence was again decreased to 3 minutes. At 3 minutes, we can more accurately identify and resolve the structure of stellar flares (Howard & MacGregor 2022). A detailed search of flare variability for stars in the TESS FFIs may provide a more statistical view of how flare rates change on long timescales, and if they can yield insights into stellar activity cycles.

5. Discussion

5.1. Correlations with Far- and Near-ultraviolet Flux

The stellar X-ray coronal emission is known to be a tracer of overall magnetic activity. Therefore, it should theoretically depend on the dynamo of the star, and on observable parameters that are related to the dynamo such as the rotational period. Empirical evidence indicates that there are distinct saturated and nonsaturated regimes for coronal X-ray emission from main-sequence stars. Specifically, stellar X-ray luminosity surveys have revealed that the saturation limit depends on the stellar rotation period. Namely, there is no evolution in $L_{\rm X}/L_{\rm bol}$ for stars with $P_{\rm rot} < 10$ days (Pizzolato et al. 2003). The rotation period is a good predictor of the X-ray luminosity for stars with longer $P_{\rm rot}$.

The FUV and NUV emission is another tracer of magnetic activity. Younger, more active stars display excess luminosity in both of these wavelengths (Shkolnik 2013). We use archival observations from the GALEX (Martin et al. 2005) to search for trends in FUV/NUV saturation and flare rate saturation, similar to the established X-ray trends. GALEX provides broad FUV photometry from 1350 to 1750 Å and NUV photometry from 1750 to 2750 Å. We crossmatch our target stars with the GALEX catalog following the sample selection methods outlined in Schneider & Shkolnik (2018). Specifically, we search using a 10″ radius around the coordinates of each target in our sample. We include targets with no bad photometric flags (e.g., `fuv_artifact` or `nuv_artifact==0`) as defined in the catalog. It is recommended by the GALEX documentation to exclude any objects with these flags associated. Additionally, we exclude targets with measured magnitudes brighter than 15, which marks the saturation limit

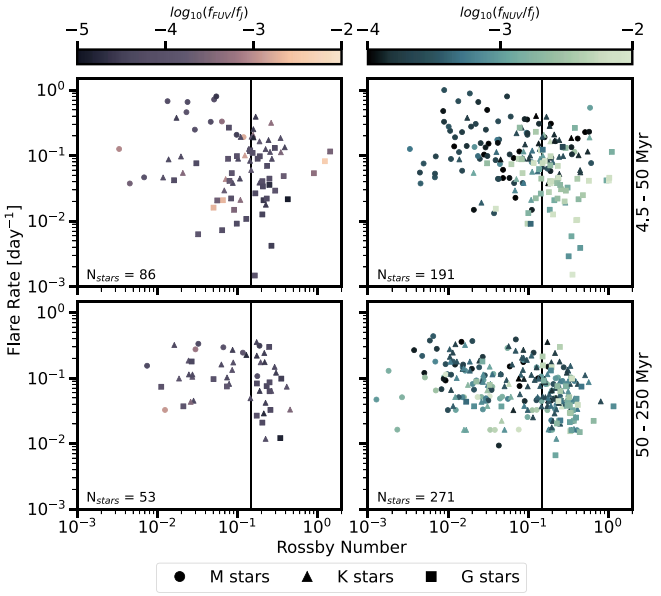

Figure 8. Calculated FUV (left) and NUV (right) GALEX flux for stars in our sample normalized by the stellar *J*-band flux. There is no obvious correlation between the fractional NUV/FUV flux and the measured flare rate or Rossby number. The top row shows GKM stars <50 Myr; the bottom row shows GKM stars ⩾50 Myr. M stars are shown as circles, K stars as triangles, and G stars as squares. We note that $f_{\rm NUV}$ traces the photosphere of G, K, and massive M stars, and therefore may not be the best comparison bandpass when looking for trends in magnetic activity.

for both the FUV and NUV photometers (Morrissey et al. 2007). Based on these thresholds, we find that 462 stars in our sample have NUV photometry and 139 stars have FUV photometry.

We investigate whether the saturation of the flare rate and FUV/NUV emission are correlated with the derived R_0 in each star. We present our results comparing the FUV and NUV flux and the measured flare rate and Rossby number in Figure 8. We present the measured FUV/NUV flux normalized by the *J*-band flux, which acts as an activity indicator. In theory, the bolometric luminosities should be a better normalization factor than the *J*-band flux. However, the majority of stars in our sample do not have bolometric luminosity measurements. Therefore, we keep the normalization to f_J while assessing FUV/NUV correlations for the larger statistical sample.

While there is tentative evidence of trends between the flare rate and the Rossby number (see Section 3.2), there is inconclusive evidence that the normalized FUV and NUV flux follow this trend. We note that the number of stars in our sample that have GALEX FUV measurements is small ($N_{\rm stars} = 139$) and therefore might not be representative of the broader population. It is worth noting that the NUV flux traces the photosphere for many of these stars, as opposed to the X-rays that trace coronal emission. Additionally, the FUV still has contributions from the photosphere for G stars. Therefore, it is possible that the lack of a correlation between the regimes identified for X-ray emission is due to the fact that the UV is tracing different stellar atmospheric regions that are not associated with the magnetic activity.

The FUV and NUV flux from GALEX is a superposition of many different emission lines. These lines trace various regions of the stellar atmosphere ranging from the corona to the photosphere depending on their formation temperatures. It is possible that the blending of lines produces a lack of correlation between the FUV/NUV flux, R_0, and the flare rate. Spectroscopic observations of targets with R_0 which span the transition out of the saturated regime may reveal a stronger relationship between these parameters. Pineda et al. (2021) reported evidence of a broken-power-law relationship between R_0 and FUV emission lines for ∼20 stars observed with the Space Telescope Imaging Spectrograph on the Hubble Space Telescope. Depending on the emission line analyzed, Pineda et al. (2021) found a saturated regime for $R_0 < 0.18$–0.24, with a steep drop-off for higher R_0. Additionally, Loyd et al. (2021) evaluated the relationship between FUV emission lines and R_0 for 12 Tucana-Horologium ($t_{\rm age} = 40$ Myr), 9 Hyades ($t_{\rm age} = 650$ Myr), and 7 field-aged ($t_{\rm age} = 2$–10 Gyr) M stars. They found a saturated $\log_{10}(R_0) = -0.876^{+0.037}_{-0.061}$, which is consistent with the X-ray flux and R_0 relationship.

The ROentgen Survey with an Imaging Telescope Array (eROSITA) instrument (Predehl et al. 2007, 2021) on the Russian Spectrum-RG mission is an all-sky X-ray survey from ∼0.2 to 8 keV. The synergies between eROSITA and TESS are already being explored. Magaudda et al. (2022), used the measured $L_{\rm X}$ from eROSITA and $P_{\rm rot}/R_0$ from TESS for 704 M dwarfs to reconfirm the known X-ray activity relationship. It is possible that these combined data may show a clearer relationship between R_0 and flare rate in the X-ray than shown here in the FUV/NUV (Figure 8).

5.2. Flare Rates of Young Planet Host Stars Versus Comparison Sample

The all-sky observing strategy of TESS has revealed a new population of young transiting exoplanets. Characterization of the environment of these planets is crucial to understanding their subsequent evolution. Specifically, the stellar environment can impact how these young planets evolve into their mature counterparts.

It is unclear whether stellar flares are beneficial or detrimental to the habitability of exoplanets. It is possible that stellar flares can trigger the development of prebiotic chemistry (Rugheimer et al. 2015; Airapetian et al. 2016; Ranjan et al. 2017; Rimmer et al. 2018). On the other hand, stellar flares and affiliated coronal mass ejections can permanently alter atmospheric compositions (Chen et al. 2021). This alteration may increase the amount of atmospheric mass stripped during the early stages of planet evolution (Feinstein et al. 2020b). Therefore, understanding the environment of young transiting exoplanets can provide insight into their evolution.

To this end, we compare the measured flare rates of young, planet-hosting stars to a statistical sample of stars with similar ages and $T_{\rm eff}$ that do not have confirmed short-period planets. Specifically, we measured the flare rates of planet-hosting stars with ages <300 Myr, comparable to the ages of our primary sample. We followed the methods outlined in Section 2 to detect and vet flares for the planet-hosting stars.

For our comparison sample, we considered stars with ages ±30 Myr of the planet-hosting star and $T_{\rm eff} \pm 1000$ K. For each of the stars in the control samples, we calculated the flare rate following Equation (3). We present the flare rates of planet-hosting stars and a comparable sample of stars in Figure 9 and report the measured rates in Table 2. For the control samples, we report the median flare rate and the lower 16th and upper 84th percentiles.

Flare rates are slightly diminished for the majority of planet-hosting stars compared to the control sample. This could be

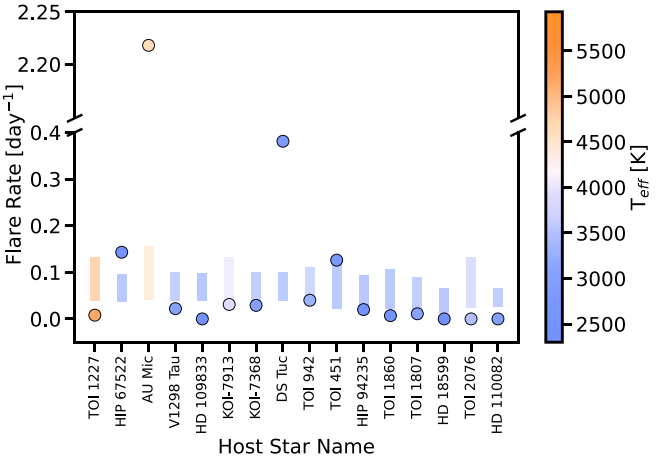

Figure 9. Comparison of flare rates from young planet host stars with respect to a comparable sample with respect to age [Myr] and $T_{\rm eff}$ [K]. Circles represent the flare rate of the host star (name along the *x*-axis); vertical bars represent the lower 16th and upper 84th percentiles for the comparable sample. The majority of young planet host stars have comparable flare rates to the lower end of the comparison sample. A handful of hosts have more flares, including HIP 67522, AU Mic, DS Tuc A, and TOI 451. We find no correlation with the spectral type or age which may indicate why these host stars are relatively flare quiet. The measured flare rates are presented in Table 2.

Table 2
Young Planet Host Flare Rates

Host Name	Age (Myr)	Flare Rate (day^{-1})	Comp. Sample Flare Rate (day^{-1})	*N*
TOI 1227	11 ± 2	0.008	$0.065^{+0.074}_{-0.042}$	168
HIP 67522	17 ± 2	0.169	$0.081^{+0.099}_{-0.043}$	368
AU Mic	22 ± 3	2.218	$0.104^{+0.188}_{-0.066}$	590
V1298 Tau	23 ± 4	0.022	$0.116^{+0.107}_{-0.07}$	300
HD 109833	27 ± 3	0.000	$0.077^{+0.097}_{-0.039}$	415
KOI-7913	36 ± 10	0.031	$0.152^{+0.165}_{-0.094}$	312
KOI-7368	36 ± 10	0.029	$0.116^{+0.107}_{-0.071}$	285
DS Tuc	45 ± 4	0.420	$0.104^{+0.104}_{-0.061}$	281
TOI 942	50^{+30}_{-20}	0.040	$0.092^{+0.146}_{-0.049}$	120
TOI 451	120 ± 10	0.128	$0.059^{+0.136}_{-0.03}$	204
HIP 94235	133^{+15}_{-20}	0.020	$0.048^{+0.094}_{-0.028}$	165
TOI 1860	133 ± 26	0.008	$0.049^{+0.108}_{-0.026}$	207
TOI 1807	180 ± 40	0.013	$0.06^{+0.11}_{-0.038}$	53
HD 18599	200^{+200}_{-70}	0.000	$0.033^{+0.066}_{-0.02}$	22
TOI 2076	204 ± 50	0.000	$0.083^{+0.122}_{-0.041}$	55
HD 110082	250^{+50}_{-70}	0.000	$0.088^{+0.045}_{-0.045}$	2

Note. *N* is the total number of stars used to calculate the comparable sample flare rate. We highlight host stars with flare rates higher than those in the comparison sample.

interpreted as evidence that the presence of planets inhibits magnetic reconnection events and activity, or that the presence of flares biases transit-detection algorithms. However, for all cases where the flare rates are diminished in the presence of a short-period planet, the difference between the flare rates is within 1σ and not statistically significant.

There are a handful of cases where stars hosting short-period planets exhibit drastically higher flare rates. The most dramatic case is for the 23 Myr AU Mic (Jeffries & Oliveira 2005; Malo et al. 2014; Mamajek & Bell 2014), where the flare rate is more than an order of magnitude higher than in the control sample. AU Mic and its transiting planets are generally considered as a benchmark laboratory for understanding the impact of stellar activity on young exoplanet atmospheres. The system hosts an extended debris disk (Kalas et al. 2004; Liu 2004; Metchev et al. 2005) along with *two* short-period transiting planets (Plavchan et al. 2020; Martioli et al. 2021; Gilbert et al. 2022). It is worth noting that this flare rate is consistent with that measured by Feinstein et al. (2022a) and Gilbert et al. (2022), and is not attributed to star-planet interactions (Ilin & Poppenhaeger 2022). In addition to this, HIP 67522, DS Tuc A, and TOI 451 all exhibit higher flare rates than the comparison sample. Colombo et al. (2022) analyzed the phase dependence of the flares on DS Tuc A with respect to both the stellar and planetary phase and found no strong evidence of star-planet interactions with DS Tuc Ab.

It is unclear what differentiates the planet-hosting systems with higher flare rates from the control sample. France et al. (2018) and Behr et al. (2023) found that planet-hosting stars are less active than an equivalent control sample of field-age stars in the UV. In Figure 9 the color of the points corresponds to the effective temperature of the star. It appears that the flare rates of the planet-hosting stars compared to the control sample are randomly distributed with respect to the effective temperature of the star. It is possible that there is a small age effect: the systems with higher flare rates are some of the youngest planet-hosting stars: HIP 67522 is 17 ± 2 Myr, AU Mic is 22 ± 3 Myr, DS Tuc is 45 ± 4 Myr, and TOI 451 is 120 ± 10 Myr. There is a slight preference for the younger systems to exhibit elevated flare rates, but this is marginal evidence at best. Future observations of these systems with elevated flare rates may reveal what causes this feature.

6. Conclusions

In this work, we present the first measured flare rates for stars <300 Myr using TESS 2 minute cadence observations. We identified 26,355 flares from 3160 stars (Figures 1 and 3). The results of our work are summarized as follows:

1. We measured the FFD slope, α, for samples of flares binned by age and $T_{\rm eff}$. We find α saturates at $\alpha = -0.6$ to -0.2 for stars younger than 300 Myr and declines after that age (Figure 4). This is the first evidence that flare rates saturate across spectral types, as do other tracers of stellar magnetic activity.
2. We measured rotation periods for 1847 stars and found that the relationship between flare rate and Rossby number, R_0, is best described as a piecewise function with a turnover at $R_0 = 0.136$ for stars $t_{\rm age} > 50$ Myr (Figure 5). Additionally, we find that stars with $R_0 \leqslant 0.136$ have a shallower FFD than stars with $R_0 > 0.136$, which is evidence of a more dominant rotational dynamo compared to the convective dynamo (Figure 6); this is consistent with results presented in Seligman et al. (2022).
3. We searched for evidence of FUV/NUV flux saturation as a function of R_0, similar to what is seen in the X-ray, by crossmatching our sample with the GALEX catalogs. We find no correlation between the FUV and NUV flux with flare rate (Figure 8). The NUV (and for the G-type stars, the FUV) flux traces the photosphere for many of the stars in our sample, unlike the X-ray which traces the corona. Spectrally resolved NUV and FUV observations

where the chromospheric emission lines can be isolated may be a more promising means of investigating this connection. Future synergies between eROSITA and TESS may reveal such relationships as well.

4. We compared the flare rates of planet-hosting young stars with a comparable sample with $t_{\rm age} = t_{\rm age,host} \pm 30$ Myr and $T_{\rm eff} = T_{\rm eff,host} \pm 1000$ K. We find that the majority of planet-hosting stars are flare inactive relative to a larger population of similar stars (although not to a statistically significant level), with the exception of HIP 67522, AU Mic, DS Tuc, and TOI 451 (Figure 9).
5. We searched for evidence of long-term stellar cycles by evaluating changes in flare rates and FFDs over five years of TESS observations. We identified 10 candidates that show potential evidence of local maxima in their stellar cycle, and one candidate that shows a decline in flare activity (Figure 7). We determine that these maxima are not due to flare-detection biases via injection-recovery tests. While we are unable to obtain stellar cycle timescales from three data points, these results highlight the insights flares can bring to understanding stellar dynamos for targets with more TESS observations (e.g., stars in the continuous viewing zones) and the use of future TESS extended missions.

Acknowledgments

We thank David Wilson for thoughtful conversations. We thank the anonymous reviewer for the insightful report, which improved the clarity and quality of this manuscript. This work made use of the open-source package, *showyourwork!* (Luger et al. 2021), which promotes reproducible publications. A.D.F. acknowledges funding from NASA through the NASA Hubble Fellowship grant HST-HF2-51530.001-A awarded by STScI. D.Z.S. is supported by an NSF Astronomy and Astrophysics Postdoctoral Fellowship under award AST-2202135. This research award is partially funded by a generous gift from Charles Simonyi to the NSF Division of Astronomical Sciences. The award is made in recognition of significant contributions to Rubin Observatory's Legacy Survey of Space and Time.

Facility: TESS.

Software: numpy (van der Walt et al. 2011), matplotlib (Hunter 2007), scipy (Virtanen et al. 2020), lightkurve banyan-Σ (Gagné et al. 2018b), astropy (Astropy Collaboration et al. 2013, 2022; Price-Whelan et al. 2018), `stella` (Feinstein et al. 2020a, 2020b), tensorflow (Abadi et al. 2016), astroquery (Ginsburg et al. 2019).

Appendix
Supplemental Material

In this appendix, we present all of our best-fit slopes and intercepts for various FFDs fit throughout this work. The fits outlined in Section 3.1 are included. We present the FFDs as a function of the energy in Figure A1 and the best fit parameters in Table A1. A hundred random draws from our MCMC fitting to these distributions are shown as orange lines. We fit each distribution with $E > 10^{29}$ erg, which roughly represents the turnover in each distribution. We do not fit the slope for $T_{\rm eff} = [3850–4440]$ K at 20–40 Myr due to our limited sample size (six stars in total). We provide the measured fractional luminosity and flare rate for our sample of eleven stars which show tentative evidence of stellar activity cycles in Table A2.

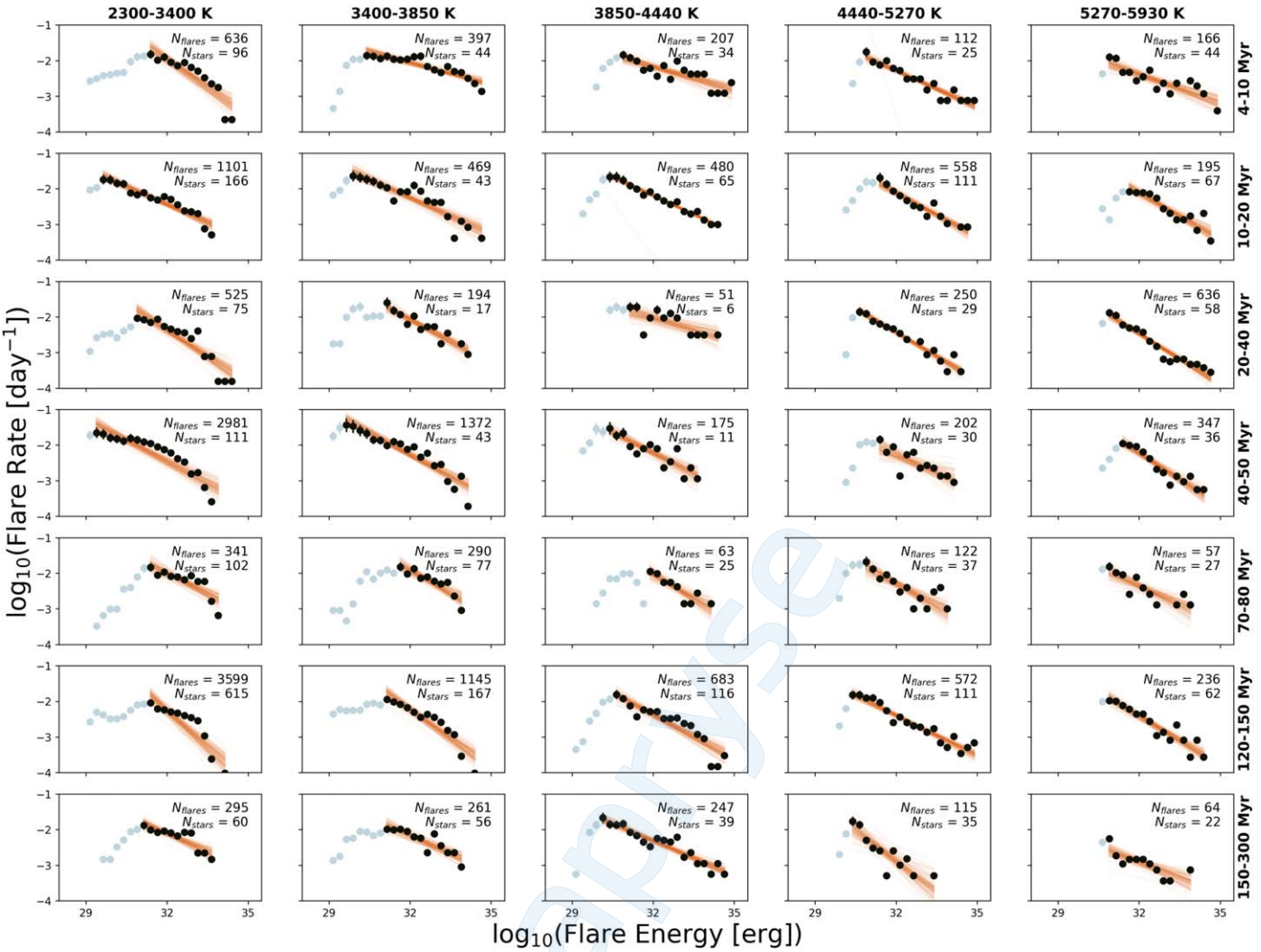

Figure A1. FFDs for subgroups of stars, clustered by age and effective temperature, $T_{\rm eff}$. Flares were sorted into 25 bins in log space from 10^{27} to 10^{35} erg. We fit the FFD from the turnover in the binned flares, likely a result of low-energy flares missed by the flare-detection algorithm. The bins used to fit the FFD are shown in black, while all bins are shown in gray. We ran an MCMC fit to these distributions with a simple power law; 100 random samples from these fits are overplotted in orange. We fit distributions with >3 bins. The best-fit slopes from these fits are presented in Figure 4.

Table A1
Best-fit Slope and Normalization Parameters for Stars of Different Temperatures and Ages

$T_{\rm eff}$ (K)	Age (Myr)	$\alpha_{\rm E}$	$\sigma_{\alpha_{\rm E}}$	$\beta_{\rm E}$	$\sigma_{\beta_{\rm E}}$	$n_{\rm E,fit}$	$N_{\rm E}$
2300–3400	4–10	−0.516	0.074	14.514	2.409	731	96
	10–20	−0.336	0.031	8.296	0.973	1183	166
	20–40	−0.499	0.058	13.564	1.858	526	75
	40–50	−0.397	0.045	10.248	1.400	3358	111
	70–80	−0.383	0.083	10.244	2.685	341	102
	120–150	−0.657	0.097	18.757	3.161	3797	615
	150–300	−0.341	0.063	8.799	2.029	295	60
3400–3850	4–10	−0.206	0.025	4.536	0.821	397	44
	10–20	−0.345	0.038	8.768	1.199	474	43
	20–40	−0.405	0.054	10.890	1.741	194	17
	40–50	−0.408	0.037	10.770	1.182	1420	43
	70–80	−0.432	0.075	11.893	2.471	291	77
	120–150	−0.525	0.062	14.557	1.998	1185	167
	150–300	−0.339	0.058	8.683	1.904	262	56
3850–4440	4–10	−0.221	0.040	4.884	1.314	207	34
	10–20	−0.350	0.016	8.998	0.545	480	65
	20–40	−0.202	0.077	4.425	2.492	51	6
	40–50	−0.379	0.062	9.873	1.982	175	11
	70–80	−0.455	0.102	12.498	3.347	63	25
	120–150	−0.419	0.046	11.010	1.494	684	116
	150–300	−0.323	0.029	8.026	0.929	247	39
4440–5270	4–10	−0.348	0.031	8.850	1.014	112	25
	10–20	−0.408	0.043	10.914	1.417	558	111
	20–40	−0.440	0.033	11.635	1.075	250	29
	40–50	−0.331	0.089	8.325	2.893	202	30
	70–80	−0.390	0.085	10.152	2.749	122	37
	120–150	−0.375	0.029	9.593	0.930	572	111
	150–300	−0.560	0.126	15.056	3.951	115	35
5270–5930	4–10	−0.271	0.049	6.280	1.586	166	44
	10–20	−0.419	0.055	11.266	1.820	195	67
	20–40	−0.465	0.035	12.377	1.149	636	58
	40–50	−0.479	0.054	13.071	1.780	347	36
	70–80	−0.337	0.083	8.416	2.656	57	27
	120–150	−0.450	0.045	11.977	1.460	236	62
	150–300	−0.305	0.081	6.826	2.598	64	22

Note. $n_{\rm E,fit}$ is the number of flares fit per bin; $N_{\rm E}$ is the number of stars in each bin.

Table A2
Evidence of Stellar Cycles from Variable Flare Properties

TIC	$\log_{10}(\xi_{\rm flare}/t_{\rm exp})$			$\mathcal{R}$ (day^{-1})		
	Year 1	Year 2	Year 3	Year 1	Year 2	Year 3
142015852	0.61	1.26	0.69	0.31	0.58	0.38
270676943	1.26	1.28	0.55	0.72	0.71	0.43
272349442	0.80	1.10	0.93	1.98	2.03	1.86
308186412	1.54	2.00	1.43	0.95	0.99	0.93
391745863	1.49	1.56	1.33	0.38	0.44	0.37
393490554	1.79	1.88	1.77	0.97	1.42	1.17
452357628	1.03	1.58	1.21	0.80	0.87	0.80
235056185	0.73	0.89	−0.41	0.74	0.61	0.24
260351540	1.09	0.78	0.46	0.24	0.15	0.09
339668420	0.30	0.83	0.37	0.28	0.53	0.16
350559457	1.15	1.38	−0.19	0.20	0.21	0.05

ORCID iDs

Adina D. Feinstein https://orcid.org/0000-0002-9464-8101
Darryl Z. Seligman https://orcid.org/0000-0002-0726-6480
Kevin France https://orcid.org/0000-0002-1002-3674
Jonathan Gagné https://orcid.org/0000-0002-2592-9612
Adam Kowalski https://orcid.org/0000-0001-7458-1176

References

Abadi, M., Agarwal, A., Barham, P., et al. 2016, arXiv:1603.04467
Airapetian, V. S., Glocer, A., Gronoff, G., Hébrard, E., & Danchi, W. 2016, NatGe, 9, 452
Argiroffi, C., Reale, F., Drake, J. J., et al. 2019, NatAs, 3, 742
Astropy Collaboration, Price-Whelan, A. M., Lim, P. L., et al. 2022, ApJ, 935, 167
Astropy Collaboration, Robitaille, T. P., Tollerud, E. J., et al. 2013, A&A, 558, A33
Bai, T. 2003, ApJ, 591, 406
Bai, T., & Sturrock, P. A. 1987, Natur, 327, 601
Barentsen, G., Hedges, C., Vinícius, Z., et al. 2019, KeplerGO/lightkurve: Lightkurve, v1.0b26, Zenodo, doi:10.5281/ZENODO.2557026
Baum, A. C., Wright, J. T., Luhn, J. K., & Isaacson, H. 2022, AJ, 163, 183
Behr, P. R., France, K., Brown, A., et al. 2023, AJ, 166, 35
Bell, C. P. M., Mamajek, E. E., & Naylor, T. 2015, MNRAS, 454, 593
Benz, A. O., & Güdel, M. 2010, ARA&A, 48, 241
Berdyugina, S. V. 2005, LRSP, 2, 8
Berger, V. L., Hinkle, J. T., Tucker, M. A., et al. 2023, arXiv.2312.12511
Bicz, K., Falewicz, R., Pietras, M., Siarkowski, M., & Preś, P. 2022, ApJ, 935, 102
Borucki, W. J., Koch, D., Basri, G., et al. 2010, Sci, 327, 977
Brasseur, C. E., Osten, R. A., Tristan, I. I., & Kowalski, A. F. 2023, ApJ, 944, 5
Candelaresi, S., Hillier, A., Maehara, H., Brand enburg, A., & Shibata, K. 2014, ApJ, 792, 67
Carrington, R. C. 1859, MNRAS, 20, 13
Chang, S. W., Byun, Y. I., & Hartman, J. D. 2015, ApJ, 814, 35
Chen, H., Zhan, Z., Youngblood, A., et al. 2021, NatAs, 5, 298
Clette, F., Svalgaard, L., Vaquero, J. M., & Cliver, E. W. 2014, SSRv, 186, 35
Crosby, N. B., Aschwanden, M. J., & Dennis, B. R. 1993, SoPh, 143, 275
Colombo, S., Petralia, A., & Micela, G. 2022, A&A, 661, A148
Curtis, J. L., Agüeros, M. A., Mamajek, E. E., Wright, J. T., & Cummings, J. D. 2019, AJ, 158, 77
Davenport, J. R. A. 2016, ApJ, 829, 23
Davenport, J. R. A., Covey, K. R., Clarke, R. W., et al. 2019, ApJ, 871, 241
Davenport, J. R. A., Hawley, S. L., Hebb, L., et al. 2014, ApJ, 797, 122
Davenport, J. R. A., Mendoza, G. T., & Hawley, S. L. 2020, AJ, 160, 36
Doyle, L., Ramsay, G., & Doyle, J. G. 2020, MNRAS, 494, 3596
Feigelson, E. D., & Montmerle, T. 1999, ARA&A, 37, 363
Feinstein, A., Montet, B., & Ansdell, M. 2020a, JOSS, 5, 2347
Feinstein, A. D., France, K., Youngblood, A., et al. 2022a, AJ, 164, 110
Feinstein, A. D., Montet, B. T., Ansdell, M., et al. 2020b, AJ, 160, 219
Feinstein, A. D., Montet, B. T., Foreman-Mackey, D., et al. 2019, PASP, 131, 094502
Feinstein, A. D., Seligman, D. Z., Günther, M. N., & Adams, F. C. 2022b, ApJL, 925, L9
Fletcher, L., Dennis, B. R., Hudson, H. S., et al. 2011, SSRv, 159, 19
Fletcher, L., Hannah, I. G., Hudson, H. S., & Metcalf, T. R. 2007, ApJ, 656, 1187
Foreman-Mackey, D., Hogg, D. W., Lang, D., & Goodman, J. 2013, PASP, 125, 306
France, K., Arulanantham, N., Fossati, L., et al. 2018, ApJS, 239, 16
France, K., Loyd, R. O. P., Youngblood, A., et al. 2016, ApJ, 820, 89
Gagné, J., Fontaine, G., Simon, A., & Faherty, J. K. 2018a, ApJL, 861, L13
Gagné, J., Mamajek, E. E., Malo, L., et al. 2018b, ApJ, 856, 23
Gaia Collaboration, Brown, A. G. A., Vallenari, A., et al. 2018, A&A, 616, A1
Gaia Collaboration, Prusti, T., de Bruijne, J. H. J., et al. 2016, A&A, 595, A1
Galindo-Guil, F. J., Barrado, D., Bouy, H., et al. 2022, A&A, 664, A70
Gilbert, E. A., Barclay, T., Quintana, E. V., et al. 2022, AJ, 163, 147
Ginsburg, A., Sipőcz, B. M., Brasseur, C. E., et al. 2019, AJ, 157, 98
Goodman, J., & Weare, J. 2010, CAMCS, 5, 65
Gryciuk, M., Siarkowski, M., Sylwester, J., et al. 2017, SoPh, 292, 77
Günther, M. N., Zhan, Z., Seager, S., et al. 2020, AJ, 159, 60
Hathaway, D. H. 2015, LRSP, 12, 4
Hawley, S. L., Davenport, J. R. A., Kowalski, A. F., et al. 2014, ApJ, 797, 121
Hawley, S. L., & Fisher, G. H. 1992, ApJS, 78, 565
Hawley, S. L., Fisher, G. H., Simon, T., et al. 1995, ApJ, 453, 464
Hilton, E. J., West, A. A., Hawley, S. L., & Kowalski, A. F. 2010, AJ, 140, 1402
Howard, W. S., & MacGregor, M. A. 2022, ApJ, 926, 204
Hunter, J. D. 2007, CSE, 9, 90
Işık, E., van Saders, J. L., Reiners, A., & Metcalfe, T. S. 2023, SSRv, 219, 70
Ilin, E., & Poppenhaeger, K. 2022, MNRAS, 513, 4579
Ilin, E., Schmidt, S. J., Davenport, J. R. A., & Strassmeier, K. G. 2019, A&A, 622, A133
Ilin, E., Schmidt, S. J., Poppenhäger, K., et al. 2021, A&A, 645, A42
Jackman, J. A. G., Wheatley, P. J., Acton, J. S., et al. 2021, MNRAS, 504, 3246
Jeffers, S. V., Kiefer, R., & Metcalfe, T. S. 2023, SSRv, 219, 54
Jeffries, R. D., & Oliveira, J. M. 2005, MNRAS, 358, 13
Jenkins, J. M., Twicken, J. D., McCauliff, S., et al. 2016, Proc. SPIE, 9913, 99133E
Kalas, P., Liu, M. C., & Matthews, B. C. 2004, Sci, 303, 1990
Kerr, R. M. P., Rizzuto, A. C., Kraus, A. L., & Offner, S. S. R. 2021, ApJ, 917, 23
Kilcik, A., Yurchyshyn, V. B., Ozguc, A., & Rozelot, J. P. 2014, ApJL, 794, L2
Kleint, L., Heinzel, P., Judge, P., & Krucker, S. 2016, ApJ, 816, 88
Kounkel, M., Covey, K., & Stassun, K. G. 2020, AJ, 160, 279
Kowalski, A. F., Hawley, S. L., Hilton, E. J., et al. 2009, AJ, 138, 633
Kowalski, A. F., Hawley, S. L., Holtzman, J. A., Wisniewski, J. P., & Hilton, E. J. 2010, ApJL, 714, L98
Kowalski, A. F., Hawley, S. L., Wisniewski, J. P., et al. 2013, ApJS, 207, 15
Kowalski, A. F., Wisniewski, J. P., Hawley, S. L., et al. 2019, ApJ, 871, 167
Krucker, S., Hudson, H. S., Jeffrey, N. L. S., et al. 2011, ApJ, 739, 96
Lawson, K. D., Wisniewski, J. P., Bellm, E. C., Kowalski, A. F., & Shupe, D. L. 2019, AJ, 158, 119
Lean, J. 1987, JGR, 92, 839
Lehtinen, J., Jetsu, L., Hackman, T., Kajatkari, P., & Henry, G. W. 2016, A&A, 588, A38
Lin, J., Wang, F., Deng, L., et al. 2023, ApJ, 958, 1
Lin, R. P., Dennis, B. R., Hurford, G. J., et al. 2002, SoPh, 210, 3
Liu, M. C. 2004, Sci, 305, 1442
Loyd, R. O. P., Shkolnik, E. L., Schneider, A. C., et al. 2021, ApJ, 907, 91
Lu, E. T., & Hamilton, R. J. 1991, ApJL, 380, L89
Luger, R., Bedell, M., Foreman-Mackey, D., et al. 2021, arXiv:2110.06271
Luhman, K. L. 2007, ApJS, 173, 104
Lurie, J. C., Davenport, J. R. A., Hawley, S. L., et al. 2015, ApJ, 800, 95
Maehara, H., Shibayama, T., Notsu, Y., et al. 2015, EP&S, 67, 59
Magaudda, E., Stelzer, B., Raetz, S., et al. 2022, A&A, 661, A29
Malo, L., Doyon, R., Feiden, G. A., et al. 2014, ApJ, 792, 37
Mamajek, E. E., & Bell, C. P. M. 2014, MNRAS, 445, 2169
Martin, D. C., Fanson, J., Schiminovich, D., et al. 2005, ApJL, 619, L1
Martioli, E., Hébrard, G., Correia, A. C. M., Laskar, J., & Lecavelier des Etangs, A. 2021, A&A, 649, A177
MAST Team 2021, TESS Light Curves—All Sectors, STScI/MAST, doi:10.17909/T9-NMC8-F686
Medina, A. A., Winters, J. G., Irwin, J. M., & Charbonneau, D. 2020, ApJ, 905, 107
Metchev, S. A., Eisner, J. A., Hillenbrand, L. A., & Wolf, S. 2005, ApJ, 622, 451
Mondrik, N., Newton, E., Charbonneau, D., & Irwin, J. 2019, ApJ, 870, 10
Morrissey, P., Conrow, T., Barlow, T. A., et al. 2007, ApJS, 173, 682
Murphy, S. J., & Lawson, W. A. 2015, MNRAS, 447, 1267
Namekata, K., Sakaue, T., Watanabe, K., et al. 2017, ApJ, 851, 91
Notsu, Y., Maehara, H., Honda, S., et al. 2019, ApJ, 876, 58
Notsu, Y., Shibayama, T., Maehara, H., et al. 2013, ApJ, 771, 127
Okamoto, S., Notsu, Y., Maehara, H., et al. 2021, ApJ, 906, 72
Oláh, K., Kővári, Z., Petrovay, K., et al. 2016, A&A, 590, A133
Orrall, F. Q., & Zirker, J. B. 1976, ApJ, 208, 618
Osten, R. A., Hawley, S. L., Allred, J. C., Johns-Krull, C. M., & Roark, C. 2005, ApJ, 621, 398
Paudel, R. R., Gizis, J. E., Mullan, D. J., et al. 2018, ApJ, 858, 55
Pecaut, M. J., & Mamajek, E. E. 2016, MNRAS, 461, 794
Pietras, M., Falewicz, R., Siarkowski, M., Bicz, K., & Preś, P. 2022, ApJ, 935, 143
Pineda, J. S., Youngblood, A., & France, K. 2021, ApJ, 911, 111
Pizzolato, N., Maggio, A., Micela, G., Sciortino, S., & Ventura, P. 2003, A&A, 397, 147
Plavchan, P., Barclay, T., Gagné, J., et al. 2020, Natur, 582, 497
Predehl, P., Andritschke, R., Arefiev, V., et al. 2021, A&A, 647, A1

Predehl, P., Andritschke, R., Bornemann, W., et al. 2007, Proc. SPIE, 6686, 668617
Price-Whelan, A. M., Sipőcz, B. M., Günther, H. M., et al. 2018, AJ, 156, 123
Ranjan, S., Wordsworth, R., & Sasselov, D. D. 2017, ApJ, 843, 110
Ricker, G. R., Winn, J. N., Vanderspek, R., et al. 2015, JATIS, 1, 014003
Rimmer, P. B., Xu, J., Thompson, S. J., et al. 2018, SciA, 4, eaar3302
Röser, S., Schilbach, E., & Goldman, B. 2016, A&A, 595, A22
Rugheimer, S., Segura, A., Kaltenegger, L., & Sasselov, D. 2015, ApJ, 806, 137
Saar, S. H., & Brandenburg, A. 1999, ApJ, 524, 295
Schmitt, J. H. M. M., Ioannidis, P., Robrade, J., Czesla, S., & Schneider, P. C. 2019, A&A, 628, A79
Schneider, A. C., & Shkolnik, E. L. 2018, AJ, 155, 122
Scoggins, M. T., Davenport, J. R. A., & Covey, K. R. 2019, RNAAS, 3, 137
Seligman, D. Z., Rogers, L. A., Feinstein, A. D., et al. 2022, ApJ, 929, 54
Shibayama, T., Maehara, H., Notsu, S., et al. 2013, ApJS, 209, 5
Shkolnik, E. L. 2013, ApJ, 766, 9
Silverberg, S. M., Kowalski, A. F., Davenport, J. R. A., et al. 2016, ApJ, 829, 129
Smith, K., Güdel, M., & Audard, M. 2005, A&A, 436, 241
Tarricq, Y., Soubiran, C., Casamiquela, L., et al. 2021, A&A, 647, A19
Tofflemire, B. M., Rizzuto, A. C., Newton, E. R., et al. 2021, AJ, 161, 171
Tovar Mendoza, G., Davenport, J. R. A., Agol, E., Jackman, J. A. G., & Hawley, S. L. 2022, AJ, 164, 17
van der Walt, S., Colbert, S. C., & Varoquaux, G. 2011, CSE, 13, 22
Vasilyev, V., Reinhold, T., Shapiro, A. I., et al. 2022, A&A, 668, A167
Vida, K., Leitzinger, M., Kriskovics, L., et al. 2019, A&A, 623, A49
Vida, K., & Roettenbacher, R. M. 2018, A&A, 616, A163
Virtanen, P., Gommers, R., Oliphant, T. E., et al. 2020, NatMe, 17, 261
Webb, D. F., & Howard, R. A. 1994, JGR, 99, 4201
Wilson, O. C. 1968, ApJ, 153, 221
Woodgate, B. E., Robinson, R. D., Carpenter, K. G., Maran, S. P., & Shore, S. N. 1992, ApJL, 397, L95
Wright, N. J., Drake, J. J., Mamajek, E. E., & Henry, G. W. 2011, ApJ, 743, 48
Wright, N. J., Newton, E. R., Williams, P. K. G., Drake, J. J., & Yadav, R. K. 2018, MNRAS, 479, 2351
Yang, K. E., Sun, X., Kerr, G. S., & Hudson, H. S. 2023a, ApJ, 959, 54
Yang, Z., Zhang, L., Meng, G., et al. 2023b, A&A, 669, A15